University of Antwerp

Master thesis

Measurement of transverse displacement effects in LVDT position sensors used in ETpf

Author:
Michiel Yzewyn

Supervisor:
Prof. Dr. Hans Van Haevermaet

A thesis submitted in fulfillment of the requirements for the degree of Master of Physics

EDF group
Department of Physics

Academic year 2022 - 2023

Michiel Yzewyn
Measurement of transverse displacement effects in LVDT position sensors used in ETpf
May 2023
Supervisor: Prof. Dr. Hans Van Haevermaet

University of Antwerp
Elementary particle physics group (EDF)
Department of Physics
Groenenborgerlaan 171
2020 Antwerp

Abstract - English

The first detection of a gravitational wave (GW) in 2015 opened a whole new window to observe the universe. However a new generation of detectors is being developed to increase detections into potentially an hourly occurrence (10^5 - 10^6 events/year), unlocking the full potential of GW astronomy. ETpathfinder (ETpf) is a proof of concept experiment to test novel technologies for the Einstein Telescope, part of the next (3rd) generation of GW detectors. For GW detectors to reach the required sensitivity, a passive and active seismic attenuation system is essential. This system consists of various pendulum stages fitted with position sensors and actuators to actively control the mirror suspension. The Linear Variable Differential Transformer (LVDT) is an axisymmetric position sensor widely used in ETpf, providing precise position measurements $\sim nm/\sqrt{Hz}$ over a large range $\sim \pm 10\,mm$, for movement along the symmetric axis. LVDTs generate a highly linear signal as a function of the measured displacement and are assumed to be insensitive to transverse motion. In this thesis the effect of transversal offsets is evaluated by simulating the output signal of the new ETpf LVDT designs. Additionally, the signal is experimentally measured for two of ETpathfinders LVDTs types. The overlapping simulation and experimental results challenge the assumption of LVDT signal invariance to transversal displacement. This can degrade the sensor's position measurement and shows care must be taken during the commissioning of the sensors.

Abstract - Nederlands

De eerste detectie van een gravitatiegolf (GW) in 2015 opende een nieuwe manier om het universum te bestuderen. Er wordt echter een nieuwe generatie detectoren ontwikkelt om het volledige potentieel van de gravitatiegolf astronomie te vervullen. ETpathfinder (ETpf) is een "proof of concept" experiment om nieuwe technologieën te testen voor de Einstein Telescoop, welke deel uitmaakt van de volgende (3de) generatie GW-detectoren. Een passief en actief seismisch attenuatiesysteem is vereist opdat GW-detectoren de nodige gevoeligheid bereiken. Dit systeem is opgebouwd uit verschillende pendule niveaus, welke zijn uitgerust met positiesensoren en actuatoren om de spiegelophanging actief te controleren. De Linear Variable Differential Transformer (LVDT) is een axiaal symmetrische positiesensor die veelvuldig gebruikt wordt in ETpf. De sensor biedt precieze positie metingen $\sim nm/\sqrt{Hz}$ over een breed bereik $\sim \pm 10\,mm$ voor bewegingen langs de symmetrische as. LVDTs genereren een hoogst lineair signaal in functie van de gemeten verplaatsing en verder wordt aangenomen dat het signaal ongevoelig is aan transversale bewegingen. In deze thesis wordt het effect van een transversale afwijking onderzocht door het uitgangssignaal van de nieuwe ETpf LVDT ontwerpen te simuleren. Voor twee van ETpathfinders LVDTs wordt het signaal ook experimenteel gemeten. De overlappende simulatie en experimentele resultaten betwisten de aanname dat het LVDT signaal volledig invariant is aan transversale uitwijkingen. Dit kan mogelijks een niet verwaarloosbaar negatief effect veroorzaken op de metingen van de positiesensor.

Acknowledgement

I'm extremely grateful to professor Hans Van Haevermaet, I couldn't have wished for a more understanding and supportive supervisor. Being able to ask questions and advice whenever by simply knocking on your door was really helpful, I learned a lot.

Thanks should also go to Kumar and Pengbo for helping me throughout the year, not only with physics problems but also explaining your native culture, this was really eye-opening. Allowing me to work in the office greatly improved my thesis experience. It was always a pleasure to be a part of the U202 crew. The great working environment was a major boon to my productivity, and motivated me to come to the office as often as possible. We had lots of interesting and useful discussions, thanks Kamiel, Max and Guillaume. I would be remiss in not mentioning the other members of the EDF group, everyone was always up for a talk during the break or while waiting in the coffee queue.

Finally, I could not have undertaken this journey without my parents. It is their unwavering support and interest in my work which allows me to finish my degree, thank you.

Contents

1 Introduction

> *Prediction is very difficult, especially about the future.*
>
> **— Niels Bohr**

Although predicted in 1916 by Einstein through the theory of General Relativity [1], it took almost 100 years to finally measure Gravitational Waves (GW) directly. The first direct observation at 14 september in 2015, called GW150914 [2], took place in the Light Interferometer Gravitational wave Observatory (LIGO), which consists of two US based detectors located in Hanford, WA and Livingston, LA respectively. Only two years after the detection, the Nobel prize was awarded to this enormous achievement.

The measurement of GWs is based on the relative change in distance between two points induced by the stretching of spacetime by the passing of a GW. This relative change is called strain and is only of the order of 10^{-21} for the most powerful GWs which reach the earth [2]. Existing GW detectors consist of modified Michelson interferometers (MITF), which exhibit a change in the interference fringes due to a relative shift in length between the two laser arms, induced by the passing of a GW. By recycling the injected laser in a Fabry-Perot cavity, the effective laser arm length can be increased, thus improving sensitivity. The $1064\ nm$ lasers are injected in an ultra high vacuum environment and reflected by suspended fused silica mirrors of $40\ kg$. The ground based detectors are sensitive to frequencies between $10\ Hz$ to $10\ kHz$.

Since the detection of GW150914, Advanced LIGO [3] and Avanced Virgo [4] (single detector situated in Italy) have detected 90 transient GWs [5]. For the next observing run (*O4*) starting on 24/05/2023, the Japan based detector KAGRA [6] is joining the LIGO-Virgo collaboration. Although numerous GWs have been observed to date, a new generation of detectors of vastly enhanced sensitivity will increase detections into potentially an hourly occurrence, unlocking the full potential of the GW science domain.

The Einstein Telescope [7] is the European project which promises to usher observations into a new era of gravitational wave astronomy. A drastic reduction of the noise in the sub-10Hz region as well as increasing the overall sensitivity, should allow for the detection of more distant and potentially new sources [8, 9] (Fig 1.4). Compared to existing MITF detectors with traditional L-shaped geometry, ET will consist of interferometers nested in a triangle[1] shape with an arm length of $10\ km$.

To achieve the required performance, R&D of new and improved technologies is essential. The ETpathfinder (ETpf) project [11, 12] has been set up in Maastricht as a testbed to

[1] An alternative possibility of two traditional L-shaped MITFs is still under study [10].

explore the key points for ET ; the usage of test masses suspended at cryogenic temperatures, made out of silicon and, new laser wavelengths. ETpf is a collaboration between universities and research institutes of Germany, The Netherlands and Belgium. The project received a 14.5M euro funding by Interreg Vlaanderen-Nederland, it is currently under construction and expected to be operational by the end of 2025. ETpf will test two Fabry-Perot Michelson Interferometer (FPMI) configurations, each with a given temperature ($120\ K$ vs $15\ K$) and respective laser wavelength ($1550\ nm$ vs $2090\ nm$). Both configurations feature test masses with a diameter of $15\ cm$ ($3\ kg$), a picture of the setup is shown in Fig. 1.1. The results from the two configurations determine the temperature and wavelength for the next stage of the project in which the setup will be transformed into one Interferometer (ITF), making use of both arms of the initial setup with test masses of $35\ cm$ diameter ($100\ kg$).

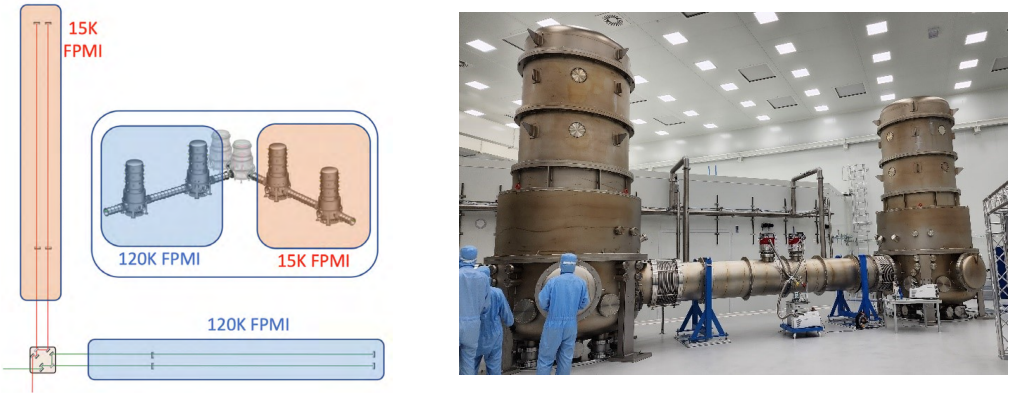

Fig. 1.1 Left panel: schematic of ETpathfinder configuration [11]. Right panel: mirror suspension towers at ETpf.

For existing interferometer GW detectors, the measured length variation is on the order of $10^{-19}\ m$ or $\sim 1/10000$ the width of a proton. The required sensitivity implies the need for external noise suppression. Therefore GW detectors contain extensive seismic attenuation systems consisting of both passive and active components. One crucial element is the Linear Variable Differential Transformer (LVDT). LVDTs are position sensors that convert linear displacement into a highly linear electrical signal through the principle of mutual induction. A linearity deviation below 1% over a dynamic range of $\pm\ 10\ mm$ is achievable [13]. The high linearity simplifies signal-processing and permits fast position readout. Another key advantage of the LVDT is its non-contact measuring capability, which prohibits vibration transfer throughout the seismic insulators and suspensions [14]. Additionally, motion transversal to the sensing axis is assumed to cause a negligible change in the output signal. Including a voice coil in the LVDT design also allows for the actuation of the required DoF. Furthermore, by measuring and actuating the position of the pendulum stages and mirrors, it is possible to control and calibrate the interferometer system of a GW detector. The simulation and characterisation of LVDTs essential for the ETpf project is the subject of this thesis. Before giving a more in depth explanation of LVDTs, a couple of sections will be dedicated to gravitational waves and other subsystems of a FPMI GW detector.

1.1 Gravitational waves

Gravitational waves are ripples in the curvature of spacetime that propagate at the speed of light [15]. Contrary to electromagnetic radiation, gravitational radiation passes almost unaffected through matter due to its weak interaction. Before the advent of GW detectors, the only means of probing the universe was through the electromagnetic spectrum and neutrino detection. As previously mentioned the measurement of GWs is based on the relative change in distance between two points. A GW will not cause any observable effect on the position of a singular particle in empty space. Figure 1.2 illustrates the effect of a gravitational wave propagating along the Z axis with a $+$ polarisation on test particles, i.e. particles at rest in empty space which are only subjected to gravity. The particle ring stretches and squeezes in a oscillating motion, alternating for the X and Y direction. Two types of GW polarisations $+$ and $\times$ can be emitted; the effect of a $\times$ polarised wave on the circular configuration will cause a similar stretching as in the illustration, rotated over 45 degrees.

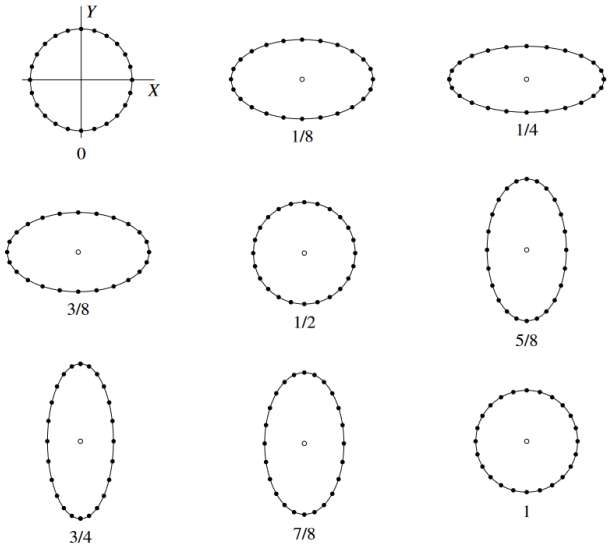

Fig. 1.2 Effect of a $+$ polarised gravitational wave propagating in the Z direction (perpendicular to X,Y-plane) on a ring of test particles for increasing fractions (0, $1/8$, $1/4$, ..) of the wave period. Picture taken from [16].

By attenuating the vibrations in the suspension of the FPMI detector, the mirrors of the laser cavities become freely falling test masses along the axis of the laser. The relative change in distance between the test masses is observed by the phase change of the two ITF beams. A perpendicular configuration of the laser arms maximizes the observable effect of the relative length change as seen in Fig. 1.2.

GW detection gives rise to the observation of previously undetected phenomena, like the merger of distant black holes and neutron stars. Furthermore, GW measurements provide novel empirical tests for General Relativity [17] as well as for the standard model of

particle physics and the Big Bang [18]. The gravitational wave detector thus provides an unprecedented look into the cosmos.

The source for the first detected GW (GW150914) is the merger of two Black Holes (BHs), also called BH-BH binaries. Two compact massive astrophysical objects like BHs and Neutron Stars (NSs) orbiting each other are called compact binaries. During the orbit the compact objects emit gravitational radiation, resulting in a loss of energy and thus a smaller orbit radius. The astrophysical objects undergo an inspiral motion, with an increasing orbit frequency. Only the last moments of GW emission before the merger of the two BHs were observed by LIGO, presented in Figure 1.3.

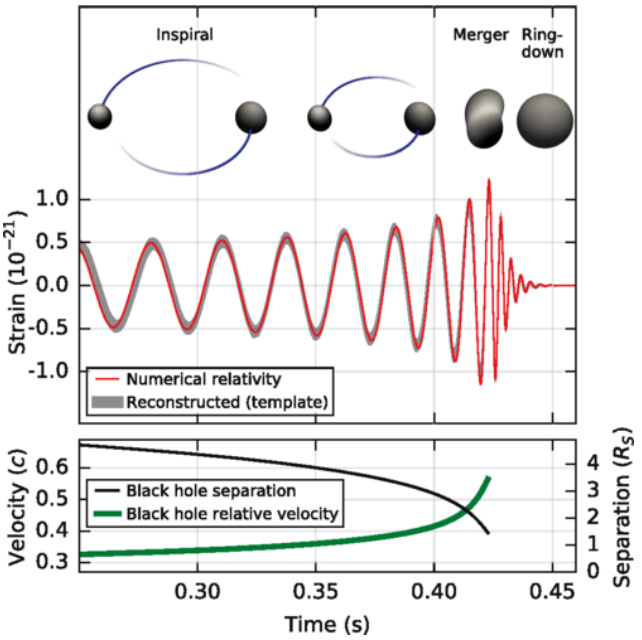

Fig. 1.3 Estimated GW strain from GW150914 projected on the reconstructed LIGO Hanford strain signal. $R_s = 2GM/c^2$ denotes the Schwarzschild radius as a function of total mass of the system M. Figure from [2].

Since the amplitude of the emitted GW strain depends on the acceleration of the compact objects, the amplitude increases drastically in the last seconds before coalescence. Years before the merger, the binary system emits a continuous sinusoidal signal with no significant change in amplitude and frequency over a duration of days. Non-axisymmetric neutron stars are also predicted to emit continuous GWs at twice their rotation frequency [19]. Detection of such a source should provide novel data on the inner workings of neutron stars and nuclear matter.

Burst signals are another type of predicted GWs; short-duration events like non-spherically symmetric supernovae or gamma ray bursts may produce detectable gravitational radiation. These systems however present considerable simulation challenges, such that the shape of a possible emitted signal remains unclear [18]. Furthermore, burst signals may be one of

the most likely sources to reveal astrophysical phenomena which have never been observed before like cosmic strings [20].

Similar to the cosmic micro-wave background a Stochastic Gravitational Wave Background (SGWB) is expected to arise from a superposition of incoherent primordial GWs created by the Big Bang. Distant binary mergers and cosmic strings signals too weak to detect individually may also generate a detectable SGWB [21]. Stochastic background searches are performed by cross correlating the strain amplitude of two GW detectors and thus present no real-time detectable signals. Hitherto no SGWB has been detected by the LIGO-Virgo detectors during the *O1-O3* observing runs [22]. Pulsar Timing Array data however suggests an indication of a possible SGWB in a frequency band not accessible by ground based MITF GW detectors [23].

The Einstein Telescope will have an order of magnitude sensitivity improvement compared to second generation detectors, presented in Figure 1.4.

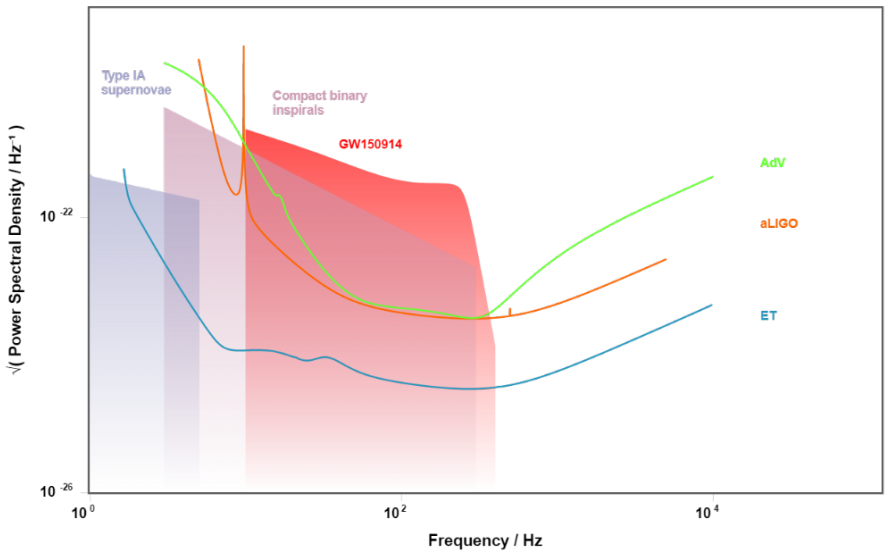

Fig. 1.4 Noise PSD of existing detectors (AdV: Advanced Virgo and aLIGO: Advanced LIGO), the predicted PSD of ET and the estimated PSD of GW sources [9].

The probed region of space will thus increase a thousandfold for the population of BH binaries observed by 2G detectors, corresponding to the detection of $10^5 - 10^6$ events per year [7]. Additionally BH binaries with a larger total system mass may be detected as well as elusive burst signals. ET will also measure GWs with an unprecedented SNR, allowing for the observation of the inspiral motion of BH/NS binaries over a larger time period providing further tests of GR. The triangular geometry of ET is equally sensitive to both GW polarizations and shows a more isotropic sensitivity compared to an L-shaped geometry. Furthermore since the Einstein Telescope consists of multiple ITFs it is possible to achieve standalone triangulation of GW sources. The increased sensitivity of ET implies cross correlating detector strain data is more likely to yield an SGWB observation. However

detection of a stochastic background by means of a cross correlation between two ET ITFs can be hampered by co-located Newtonian noise [24].

1.2 Detector Optics

All interferometer GW detector optical designs are based on a modified MITF with kilometer scale Fabry-Perot resonant cavities. Since specific modifications may differ between detector designs, this explanation will be based on the design of Advanced Virgo [25]. Figure 1.5 shows a general overview of the optical layout in AdV. This picture omits various components, showing only the main systems which make up the optical design of AdV.

The interferometer starts with a $200\ W$ $1064\ nm$ high power fiber amplified laser, which is stabilized in power, frequency and in beam pointing [26]. The beam passes through the Input Mode Cleaner (IMC), which stabilizes the mode content of the laser. The laser beam at the output of the IMC has $125\ W$ remaining in the TEM_{00} mode, which then enters the core optics by passing through the Power Recycling Mirror (PRM). The beam splits in the Beam Splitter (BS) and enters the interferometer arms resonant cavities after the Compensation Plate (CP). The CP allows for thermal compensation for the Input Mirror (IM). The End Mirror (EM) and IM are concave mirrors, also known as test masses that make up the Fabry-Perot cavity with an arm length of $3\ km$. Behind the EM another mirror is attached as a reaction mass for the endpoint of the cavity. The arm cavities have a finesse of 440, such that the IM transmission is set to 1.4% and the EM is completely reflective up to transmission of a few ppm. The low transmission of the IM results in $700\ kW$ of laser power being stored in the cavities. The light exiting the cavities propagates to the Signal Recycling mirror (SRM) by being partially reflected by the BS. Part of the beam passes the SRM and enters the Output Mode Cleaner (OMC) which serves a similar purpose as the IMC for the output signal. After purifying the modes of the output signal, the beam is passed to the photodetector B1. The Beam is locked on the dark fringe of the interference pattern, corresponding to destructive interference, such that length perturbations in the arm length will shift the fringes, resulting in light hitting the photodetector.

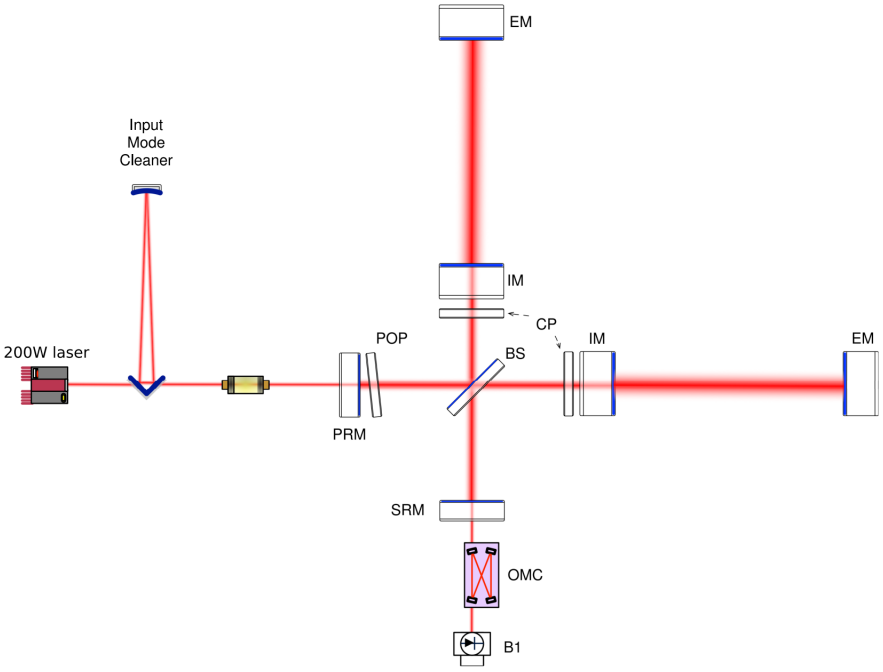

Fig. 1.5 Simplified optical layout of Advanced Virgo from [27].

The first stage of ETpf will feature an ITF configuration similar to Advanced Virgo [11] with an injected laser power of $2\,W$, however no recycling cavities will be present and the laser arms geometry is parallel instead of perpendicular for each respective wavelength ($1550\,nm$ vs $2090\,nm$) FPMI configuration shown in Figure 1.1. Many of the optical elements for $1550\,nm$ are readily available since they are essential in telecommunications, this is not the case for $2090\,nm$ which will complicate development.

To ensure that GWs are the only perturbations causing the shift of the interference fringes, all mirrors and optical benches/stages need to be isolated from external noise and vibrations. A part of the noise isolation is done actively by means of a feedback loop making use of LVDTs. Furthermore the optical cavities are locked using active control loops which require transducers like LVDTs.

1.3 Suspension and isolation

ETpathfinder will use varying designs of multi-stage vibration attenuators depending on the noise requirements for the isolated component. For the cryogenically cooled mirrors of the arm cavities a noise floor of $10^{-18}m/\sqrt{Hz}$ is targeted in the $10\,Hz$ to $10\,kHz$ band [11]. These components will be suspended by long attenuation chains based on Virgo and KAGRA designs [28, 29]. The Beam-splitters and input mode-cleaners optics which are not cooled have less stringent noise requirements of $10^{-15}m/\sqrt{Hz}$.

The noise isolators consist of various basic "building blocks" configured for the given optical component. All attenuation towers start with an inverted pendulum (IP) platform, which is made up of three legs mounted on a stiff base supporting the top platform. An IP leg consists of elastic flexures inside hollow cylinders at the top and bottom of the leg connected by a rigid rod upholding a load mass at the top [30]. The mass in addition to the flexure stiffness allows for the tuning of the resonant frequency $f_0 \leq 100\,mHz$ of the oscillating system, providing passive attenuation in the horizontal plane for $f \gg f_0$.

Since vertical motion is coupled to horizontal motion, i.e. the measured DoF, noise reduction in the vertical direction is mandatory. The Geometric Anti-Spring (GAS) filter is another basic noise isolator component, which provides isolation in the vertical DoF. The isolation is achieved by means of the geometric anti-spring effect that makes use of horizontally compressing springs to lower the vertical stiffness of the oscillating system [31], see the left panel of Figure 1.6. This allows for the adjustment of the eigenfrequency and attenuation in the desired frequency range. Practically the GAS filter is realized by radially connecting cantilever blades in a central disk (keystone) shown in the right panel of Figure 1.6. The compression of the blades can be regulated by adjusting the radial clamp position. Resonant frequencies of $\sim 0.2\,Hz$ to $0.3\,Hz$ are attainable, resulting in a damping of $\sim\ 6$ orders of magnitude above $10\,Hz$. Furthermore, mounting an LVDT and voice coil to the keystone allows for the monitoring and control of the vertical position of the filter. Additional LVDTs and actuators can be integrated into the filter design to control the horizontal translational (x, y) and rotational (yaw) DoF.

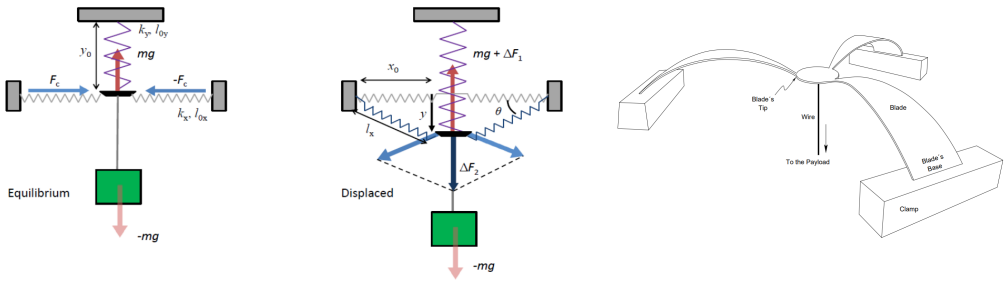

Fig. 1.6 Left panel: Illustration of GAS effect from [32]. Right panel: Simplified picture of GAS filter example from [33].

A wire is suspended by the keystone of the GAS filter, which acts as a pendulum, attenuating noise in the horizontal plane. The pendulum itself can carry a GAS filter, yielding further vertical attenuation. Multiple pendulums are connected in a chain to achieve the required isolation. The final isolation pendulum will suspend a marionette carrying a mirror or optical bench depending on the tower design. LVDTs, optical levers and other sensors measure all the DoF of the given payload. Actuation is enabled by voice coils, step motors, ... The marionette is used for the positioning of the mirrors in the rotational DoF, see Figure 1.7.

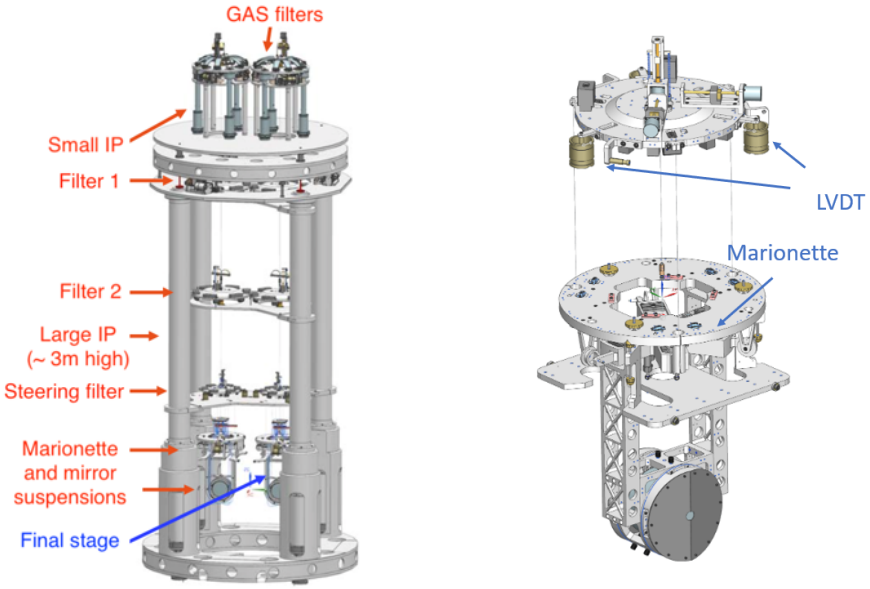

Fig. 1.7 Left panel: Mirror attenuation tower ETpf. Right panel: Mirror suspension and marionette for $123K$ system. Pictures from [11].

1.4 ITF control

Within Etpf control loops exist on multiple levels such as local control for a single suspension tower, a global control system and which regulates the position of multiple mirrors necessary to lock the interferometer, fast dedicated control loops with a single input and output to stabilize laser frequency, laser amplitude, etc. A final general type of a control loop are slow automation loops which for example adjust the parameters of the faster local, global and dedicated control loops due to temperature shifts and other environmental factors. Figure 1.8 shows an example of a typical control system.

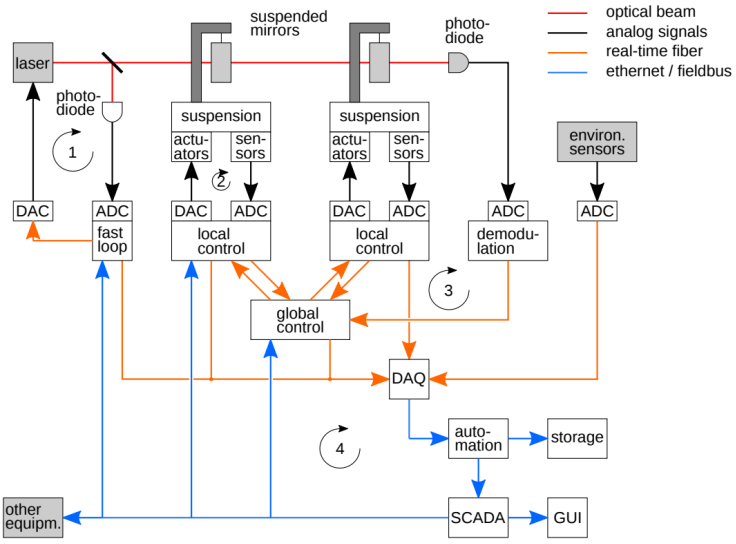

Fig. 1.8 Typical control system for an ITF GW detector. The circle arrows denote the levels of control loops: 1) fast dedicated loops, 2) local control, 3) global control and 4) general slow automation loops. Illustration from [11].

The dynamics of the suspension of a single mirror are measured by 40-50 sensors, for which around 10-20 actuators are used to stabilize the system. The required local control loop will thus be a Multiple Input Multiple Output (MIMO) control system. LVDTs make up a large portion of the sensors for the local control which provide the necessary real-time position measurement capabilities. The control system measures the position of the various pendulum stages. Any undesired displacement is corrected by actuating the stages in the opposite direction, cancelling the offset. ETpathfinder introduces various new LVDT designs used throughout the experiment. The left panel of Figure 1.9 illustrates the number of LVDTs used in the ETpf mirror and bench towers in the different suspension stages. The right panel shows a type A LVDT installed on an inverted pendulum prototype.

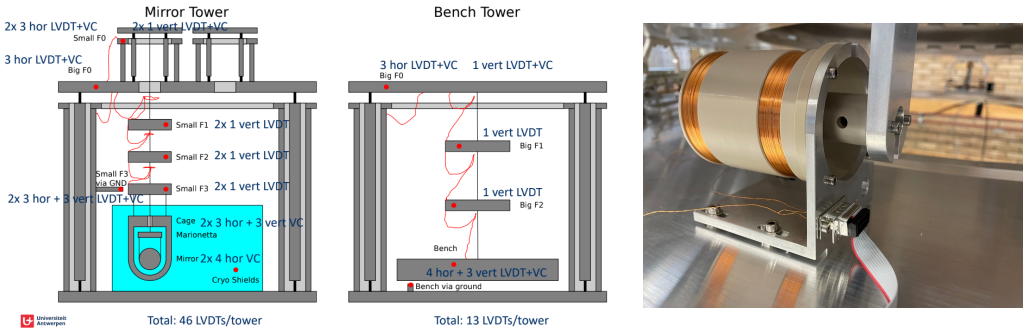

Fig. 1.9 Left panel: overview of mirror and bench tower horizontal (hor) and vertical (ver) LVDTs with integrated voice coils (VC) for ETpf. Right panel: type A LVDT installed on an inverted pendulum prototype.

2 LVDT

The LVDTs in ETpathfinder consist of three coils, the smallest coil called the *inner coil* is mounted to the object of which the relative position is measured. The two *outer coils* attached to a reference structure are wound oppositely and share the same central z axis as the inner coil, shown in Figure 2.1. Exciting the inner coil with a sinusoidal signal (of $10\,kHz$) generates an oscillating magnetic field. Making use of the Biot-Savart law [34] for an electromagnetic coil:

$$\mathbf{B}(z) = N\frac{\mu_0 I(t) R^2}{2(z^2+R^2)^{3/2}}\mathbf{e}_z \tag{2.1}$$

which relates the magnetic field $\mathbf{B}(\mathbf{z})$ induced by a tightly wound coil along its symmetric axis to the distance from the coils center z, the number of windings N, the radius of the coil R and the current running through the windings $I(t)$. The constant μ_0 denotes the vacuum magnetic permeability. For an oscillating input current $I(t) = Isin(\omega t)$ the generated magnetic field of eq. (2.1) indeed oscillates at the same frequency. The magnetic field generated by the inner coil passes through the outer coils. Following the universal flux rule [34]:

$$\mathcal{E} = -\frac{d\Phi_B(t)}{dt} \tag{2.2}$$

an electromotive force (emf) $\mathcal{E}$ or voltage V is induced in both outer coils: V_{upp} and V_{low} by the changing magnetic flux $\Phi_B(t)$ enveloped by the coils. The magnetic flux is related to the magnetic field via:

$$\Phi_B(z,t) = \int_\Sigma \mathbf{B}(z,t).d\mathbf{S} \tag{2.3}$$

where Σ denotes the boundary of the coil surrounding the integration area and $d\mathbf{S}$ the infinitesimal surface element, oriented perpendicular to the integration surface. The magnetic flux produced by an oscillating magnetic field $\mathbf{B}(z,t) = \mathbf{B}(z)sin(\omega t)$ will similarly oscillate. The oscillating flux in the outer coils in turn induces an oscillating emf following the flux rule. The amplitude of the induced voltage in a given outer coil depends on the vertical position of the inner coil z, reaching a maximum when its center coincides with the inner coil's center. Connecting the outer coils in series allows for the evaluation of the induced voltage difference $V_{diff} = V_{upp} - V_{low}$. This voltage difference serves as a measurement for the relative position of the inner coil, reaching $0\,V$ when the inner coil is in the vertical midpoint between the two outer coils. Counter winding the outer coils implies the sign/phase of V_{diff} changes depending on which is nearest to the inner coil. Figure 2.2 shows an example of

inner and outer coil signals for a type A LVDT. The upper outer coil signal is in phase with the inner coil signal, in the lower outer coil a signal in antiphase is generated. The inner coil position of $z = 1\ mm$ is closer to the upper outer coil than the lower outer coil, therefore the upper outer coil signal has higher amplitude than the lower outer coil signal, resulting in a net differential outer coil voltage in phase with the excitation signal.

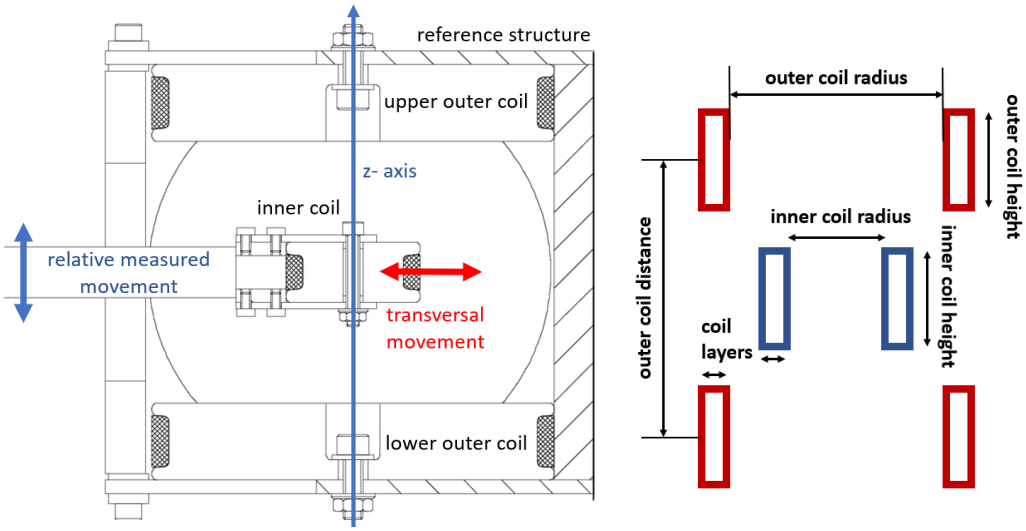

Fig. 2.1 Left panel: cutaway overview of an LVDT [13]. Right panel: dimensions LVDT design.

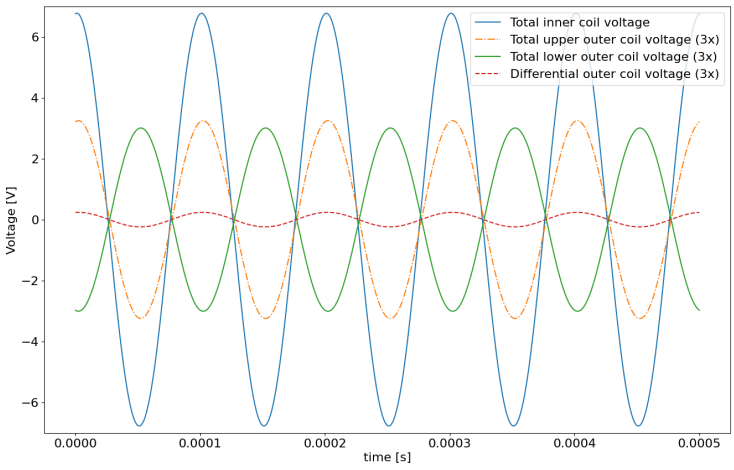

Fig. 2.2 Simulated signal of a type A LVDT with an inner coil position of $z = 1\ mm$ excited at $10\ kHz$. The upper, lower and differential outer coil voltages are increased by a factor 3 for illustrative purposes.

The LVDT can be interpreted as an electric circuit with coupled coils due to mutual induction. Mutual inductance M is a measure of the voltage induced in a coil due to a changing current

in another coil [35]. The mutual inductance is related to the self inductance L which links the induced voltage in a coil $V(t)$ caused by a changing current $I(t)$ in the same coil:

$$V(t) = L\frac{dI(t)}{dt}. \tag{2.4}$$

The behavior described by equation (2.4) is a consequence of the universal flux rule (eq. (2.2). A circuit with a changing magnetic flux caused by a changing current in the given circuit induces a emf opposing the change of flux. The dynamics of an electric circuit for coupled coils with a mutual inductance M and self-inductances L_1 and L_2 for coil 1 and 2 respectively, can be described by

$$V_1(t) = L_1\frac{dI_1(t)}{dt} - M\frac{dI_2(t)}{dt}. \tag{2.5}$$

$V_1(t)$ denotes the voltage in coil 1, $I_1(t)$ and $I_2(t)$ denote the currents in the respective coils. Furthermore the mutual inductance M is related to L_1 and L_2 via equation (2.6).

$$M = k\sqrt{L_1 L_2} \tag{2.6}$$

The coupling coefficient k is a purely geometric factor, dependent on the sizes, shapes and relative positioning of the coupled coils. Practically k can only be derived from numerical computations. The signals in an LVDT due to a coupled inner and outer coil can be analysed using equation (2.5) once L_1, L_2 and k are known. If one wants to investigate the behavior of the LVDT circuit (consisting of the coupled inner and outer coils) as a function of the inner coil position z, the coupling factor needs to be derived for each evaluated z position.

One of the main features of an LVDT is its highly linear output signal, which is achieved by a Maxwell Pair (MP) configuration [13]. The MP maximizes the uniformity of the gradient of the magnetic field $\frac{d\mathbf{B}}{dz}$. A conventional Maxwell pair is composed of two coils with radii R and a distance d apart from each other, which generate opposing magnetic fields in the center between the coils. For LVDTs the field is generated by the inner coil which generates an emf in the outer coils, resulting in an inverted MP. Maxwell Pairs and LVDTs have a typical relation between the radius R and distance d of the outer coils to achieve maximal uniformity of the magnetic field gradient or linearity in the differential outer coil signal respectively. The relation of the dimensions is derived for the simplified case of a single inner and upper/lower outer coil winding. The single inner coil winding generates a dipole moment $m_d = \pi I R_i^2$ with I the current running through the coil with radius R_i. Figure 2.3 shows a magnetic dipole m_d (inner coil) at a distance z to an outer coil with radius R. r denotes the displacement vector from the dipole to the outer coil at an angle θ.

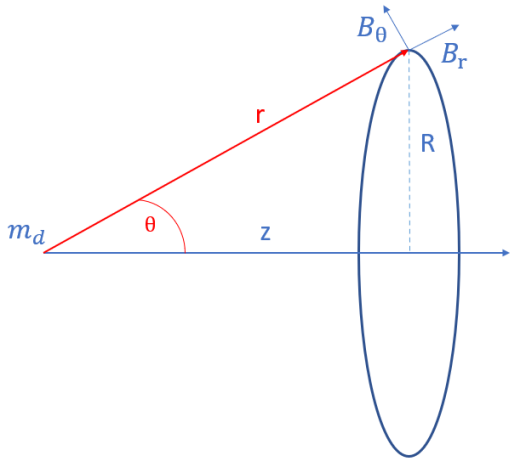

Fig. 2.3 Magnetic dipole m_d at distance z to an outer coil with radius R.

Assuming the outer coil is located far from the inner coil, i.e. $z >> R_i$ results in a magnetic field experienced by the outer coil with components given by equation (2.7) [36].

$$\begin{aligned} B_r &= \frac{\mu_0}{2\pi} m_d \frac{\cos\theta}{r^3} \\ B_\theta &= \frac{\mu_0}{4\pi} m_d \frac{\sin\theta}{r^3}. \end{aligned} \tag{2.7}$$

It can be shown that integrating the magnetic field (eq. (2.3)) to compute the magnetic flux through the outer coil Φ_o yields [37]:

$$\Phi_o(\theta) = \frac{\mu_0}{2R} m_d \sin^3\theta. \tag{2.8}$$

The variable θ of equation (2.8) can be changed to coordinate z by using $r\sin\theta = R$ and $r = \sqrt{z^2 + R^2}$:

$$\begin{aligned} \Phi_o(z) &= \frac{\mu_0}{2R} m_d \frac{R^3}{r^3} \\ &= \frac{\mu_0}{2} m_d \frac{R^2}{(z^2 + R^2)^{3/2}}. \end{aligned} \tag{2.9}$$

Assuming the inner coil is located at $z = 0$ and the upper and lower outer coils are positioned at $z = d/2$ and $z = -d/2$ respectively, the flux in the upper outer coil is found as

$$\Phi^{+d/2}(z) = \frac{\mu_0 m_d R^2}{2((\frac{1}{2}d - z)^2 + R^2)^{3/2}} \tag{2.10}$$

similarly at $z = -d/2$ for the lower outer coil

$$\Phi^{-d/2}(z) = \frac{\mu_0 m_d R^2}{2((\frac{1}{2}d + z)^2 + R^2)^{3/2}}. \tag{2.11}$$

Both expressions eq. (2.10) and eq. (2.11) can be expanded into Taylor series, assuming only small deviations from the center, i.e. $z \approx 0$. Expanding the flux for the coil located at $z = d/2$ around $z = 0$:

$$\begin{aligned}\Phi^{+d/2}(z)|_{z=0} \approx 4\mu_0 m_d R^2 \Big(& \frac{1}{(d^2+4R^2)^{3/2}} + \frac{6d}{(d^2+4R^2)^{5/2}} z \\ & + \frac{24(d^2-R^2)}{(d^2+4R^2)^{7/2}} z^2 + \frac{96d(d^2-3R^2)}{(d^2+4R^2)^{9/2}} z^3 + \Theta(z^4) \Big).\end{aligned} \tag{2.12}$$

For the coil at $z = -d/2$:

$$\begin{aligned}\Phi^{-d/2}(z)|_{z=0} \approx 4\mu_0 m_d R^2 \Big(& \frac{1}{(d^2+4R^2)^{3/2}} - \frac{6d}{(d^2+4R^2)^{5/2}} z \\ & + \frac{24(d^2-R^2)}{(d^2+4R^2)^{7/2}} z^2 - \frac{96d(d^2-3R^2)}{(d^2+4R^2)^{9/2}} z^3 + \Theta(z^4) \Big).\end{aligned} \tag{2.13}$$

The magnetic flux is related to the induced emf in a coil via (2.2). Proving the difference between the flux in the upper outer coil and lower outer coil is linear as a function of inner coil position z, also proves the voltage difference V_{diff} is linear as a function of z. Since the coils are counter wound the fluxes can be subtracted using eq. (2.13) from eq.(2.12), which yields

$$\begin{aligned}&\Phi^{+d/2}(z)|_{z=0} - \Phi^{-d/2}(z)|_{z=0} \\ &\approx 48\mu_0 m_d d R^2 \Big(\frac{1}{(d^2+4R^2)^{5/2}} z + \frac{4(d^2-3R^2)}{(d^2+4R^2)^{9/2}} z^3 + \Theta(z^5) \Big).\end{aligned} \tag{2.14}$$

The z^3 term can be eliminated by setting the distance $d = \sqrt{3}R$:

$$\Phi^{+d/2}(z)|_{z=0} - \Phi^{-d/2}(z)|_{z=0} \approx 48\sqrt{3} \frac{\mu_0 m_d}{(7R)^{5/2}} z + \Theta(z^5) \Big). \tag{2.15}$$

Equation (2.15) shows the flux difference and therefore the voltage difference of the outer coils is linear up to $\Theta(z^5)$ order for small inner coil position deviations $z \approx 0$ if the outer coil distance d is related to the outer coil radius R by $d = \sqrt{3}R$. The derivation makes non realistic assumptions such as an inner and outer coil consisting of singular windings as well as the outer coils being located at large distances compared to the inner coil radius. The $d = \sqrt{3}R$ relation provides a rough guiding line for designing an LVDT with a highly linear differential outer coil signal.

The LVDT designs of ETpf have varying dimensions depending on its use case, not exactly following the $d = \sqrt{3}R$ relation. For example type A LVDTs will be used in the large IP to measure horizontal movement over a large range $\pm\, 10\, mm$. Type F LVDTs will provide vertical measurement over a $\pm\, 1\, mm$ range. For this reason the linearity of type A has been optimized for a larger range compared to type F. Type F in return exhibits a higher response, improving the SNR. A position resolution of $\sim nm/\sqrt{Hz}$ is targeted for both designs. Dimensions as shown in the left panel of Fig. 2.1 are provided in Table 2.1.

Type	inn height	inn rad.	out height	out rad.	out dist.	inn lay.	out lay.
F	18mm	21mm	13.5mm	31.5mm	14.5mm	6	5
A	24mm	11mm	13.5mm	35mm	54.5mm	6	5

Tab. 2.1 Type F and type A LVDT design dimensions. Inn/out height = inner/outer coil height, inn/out rad. = inner/outer coil radius, out dist. = outer coil distance, inn/out lay. = inner/outer coil layers.

The effect of transverse displacement is assumed to be negligible in an optimal operating space of $\sim$ 20 % of the volume of the LVDT [13]. The position sensor is insensitive to transversal motion when the inner coil is located in the vertical center $z = 0\,mm$ due to symmetry. However transversal displacement will modify V_{diff} when the inner coil is offset from the z midpoint. The unconventional dimensions of the type F and A design may prove to be more sensitive to transversal movement than expected. The significance of this effect is the main question to be answered in this thesis.

3 Simulation

Simulation of the LVDT is performed using a Finite Element Method (FEM) [38] in the software Finite Element Method Magnetics (FEMM) [39] by using the *pyFEMM* [40] interface to Python. FEMM allows for the modellation of 2D systems in planar and axisymmetric domains. The software can solve electrostatic and magnetostatic as well as low frequency (sub radio frequency) electromagnetic problems.

3.1 FEMM differential equations

To derive the magnetostatic differential equation solved by the FEM, several Maxwell equations are used as well as other electromagnetic equations following the FEMM documentation. Using the relationships of the field intensity $\mathbf{H}$, flux density $\mathbf{B}$ and current density $\mathbf{J}$:

$$\nabla \times \mathbf{H} = \mathbf{J} \tag{3.1}$$

$$\nabla . \mathbf{B} = 0 \tag{3.2}$$

$\mathbf{B}$ is proportional to $\mathbf{H}$ with a factor μ the magnetic permeability, such that:

$$\mathbf{B} = \mu \mathbf{H}. \tag{3.3}$$

It should be pointed out that this is only the case for linear magnetic materials, otherwise the permeability depends on $\mathbf{B}$. FEMM is able to address non linear materials but these are of no importance for the simulations in question. Introducing the vector potential $\mathbf{A}$ via

$$\mathbf{B} = \nabla \times \mathbf{A} \tag{3.4}$$

allows for the substitution of (3.4) into (3.1) which also satisfies (3.2)

$$\nabla \times \left(\frac{1}{\mu} \nabla \times \mathbf{A} \right) = \mathbf{J} \tag{3.5}$$

assuming the Couloumb gauge $\nabla . \mathbf{A} = 0$ this reduces to

$$-\frac{1}{\mu} \nabla^2 \mathbf{A} = \mathbf{J}. \tag{3.6}$$

For our purposes LVDTs are excited at a frequency of $f = 10\,kHz$. For this kind of problem FEMM assumes time-harmonic magnetic fields, i.e. magnetic fields oscillating at a fixed frequency. The differential equation solved by FEMM can be derived from:

$$\nabla \times \mathbf{E} = -\frac{\partial \mathbf{B}}{\partial t} \tag{3.7}$$

with $\mathbf{E}$ and $\mathbf{B}$ denoting the electric and magnetic field respectively. Rewriting $\mathbf{B}$ in terms of the vector potential yields:

$$\nabla \times \mathbf{E} = -\nabla \times \dot{\mathbf{A}}. \tag{3.8}$$

Integrating both sides in 2D leads to:

$$\mathbf{E} = -\dot{\mathbf{A}} - \nabla V \tag{3.9}$$

with V the scalar voltage potential. For electrically conducting materials a current will flow, in which case the current density $\mathbf{J}$ can be found by Ohm's law:

$$\mathbf{J} = \sigma \mathbf{E} \tag{3.10}$$

where σ denotes the material-dependent conductivity. Substituting (3.10) into (3.9) and adding a current source term $\mathbf{J}_{src}$:

$$\mathbf{J} = -\sigma(\dot{\mathbf{A}} + \nabla V) + \mathbf{J}_{src}. \tag{3.11}$$

Finally plugging this into (3.6) results in:

$$-\frac{1}{\mu_{eff}} \nabla^2 \mathbf{A} = -\sigma(\dot{\mathbf{A}} + \nabla V) + \mathbf{J}_{src} \tag{3.12}$$

FEMM uses an effective permeability μ_{eff} for sinusoidal fields which adjusts the DC μ. Since the $\mathbf{B}$ field is assumed to be oscillating at a fixed frequency, the same assumption is made for the vector potential and current, i.e.

$$\begin{aligned} \mathbf{A} &= \mathrm{Re}(\overline{\mathbf{A}} e^{i\omega t}) \\ \mathbf{J} &= \mathrm{Re}(\overline{\mathbf{J}} e^{i\omega t}) \end{aligned} \tag{3.13}$$

where $\overline{\mathbf{A}}$ and $\overline{\mathbf{J}}$ are the complex amplitudes of the oscillating vector fields and $\omega = 2\pi f$. Imposing the transformation on (3.12) yields:

$$\begin{aligned} -\frac{1}{\mu_{eff}} \nabla^2 \overline{\mathbf{A}} e^{i\omega t} &= -\sigma(\overline{\mathbf{A}} i\omega e^{i\omega t} + \nabla V) + \overline{\mathbf{J}}_{src} e^{i\omega t} \\ \Rightarrow -\frac{1}{\mu_{eff}} \nabla^2 \overline{\mathbf{A}} &= -\sigma(i\omega \overline{\mathbf{A}} + \nabla V) + \overline{\mathbf{J}}_{src}. \end{aligned} \tag{3.14}$$

The last equation from eq.(3.14) shows the partial differential equation FEMM solves for oscillating magnetic fields. The term ∇V is a constant integration factor which can be added at the end of eq. (3.14). The PDE is in terms of the vector potential, which is computed

using the finite element method. From the vector potential solution $\mathbf{A}$ the $\mathbf{B}$ and $\mathbf{H}$ can be found using the known relations eq. (3.4) and eq. (3.3). FEMM uses complex values to track the phase of the simulated quantities, therefore the modulus of the voltage and current needs to be taken in order to acquire the respective amplitudes.

A finite element method divides the simulated space into a large number of small subregions, effectively reformulating the differential equation for a complex problem into a large number of less complex problems. FEMM uses the shape of triangles for the subregions, the differential equations in the triangles are solved by numerical linear algebra techniques. Using the solutions for the P.D.E's at the vertices of a triangle allows for a linear interpolation of the field solution throughout the interior of the triangle.

3.2 FEMM LVDT modelling

LVDTs are simulated in the axisymmetric r, z-plane with r being the radial direction and z the vertical direction. The plane is divided into regions and for each region the given material properties are assigned. The LVDT system is enveloped in an air sphere with a radius of $300\ mm$. All fields are assumed to be negligible at this radius and a Dirichlet boundary condition is imposed at the edge of the sphere by setting the vector potential $\mathbf{A} = 0$ to keep magnetic flux from crossing the boundary. The space outside the sphere is not simulated.

A coil is modelled by drawing a rectangle with a given coil height, coil width, i.e. the wire thickness times the number of layers and specifying the number of turns per layer. The total LVDT system is constructed as presented in te right panel of Fig. 2.1. Table 2.1 shows the parameters for the respective coils and LVDT designs. The coils are wound using *32 AWG* copper wire which has a diameter of $0,2032\ mm$ and an insulation width of $0.0178\ mm$.

In FEMM the inner coil is excited by an oscillating current of $20\ mA$ and moved to various vertical positions, i.e. inner coil positions z (referring to the position of the center of the inner coil). Fig 3.1 shows an example of an FEMM LVDT simulation of type F with shifted inner coil position.

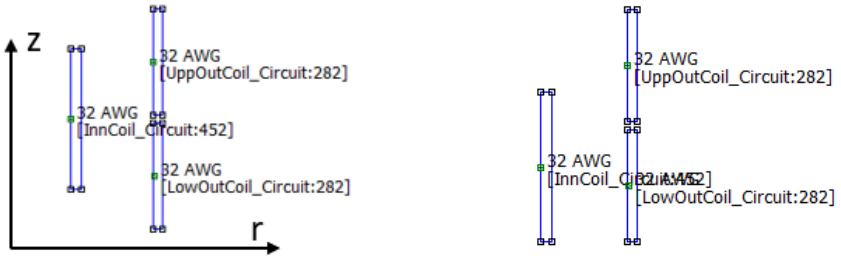

Fig. 3.1 Example FEMM LVDT simulation of type F in the r, z-plane. InnCoil denotes the inner coil, Upp/LowOutCoil the upper/lower outer coils. The total number of windings in a coil are shown behind the name. Left panel: inner coil is at center position $z = 0\ mm$. Right panel: inner coil shifted to position $z = -5\ mm$.

By evaluating the induced voltage in the outer coils at varying inner coil positions it is possible to construct an LVDT outer coil signal curve. This curve shows the differential voltage signal $V_{diff} = V_{upp} - V_{low}$ in function of the inner coil position. To account for V_{upp} and V_{low}'s linear dependency on the excitation current I_{exc}, the induced voltages are normalised, i.e. divided by I_{exc} to obtain units of V/A. Figure 3.2 shows the simulated outer coil voltages for varying inner coil positions. Subtracting the simulated lower outer coil voltage V_{low} from the upper outer coil voltage V_{upp} results in voltage difference V_{diff}, presented in Figure 3.3. The response m is a measure for the slope of the V_{diff} curve, which can be found by performing a linear fit on the data points. The normalised response in units of V/Amm gives an indication of the ability to distinguish a change in position of the inner coil.

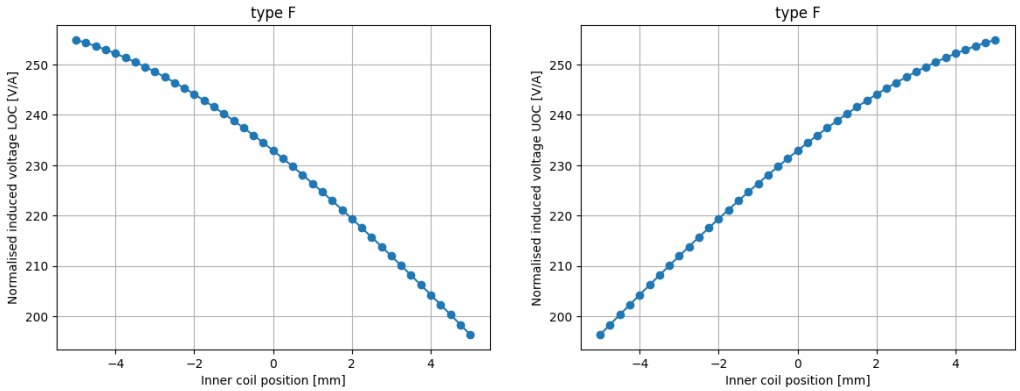

Fig. 3.2 FEMM simulated voltages for a type F LVDT for inner coil positions over $z = \pm 5\ mm$ with a stepsize of $0.25\ mm$. Left panel: normalised Lower Outer Coil (LOC) voltage. Right panel: normalised Upper Outer Coil (UOC) voltage.

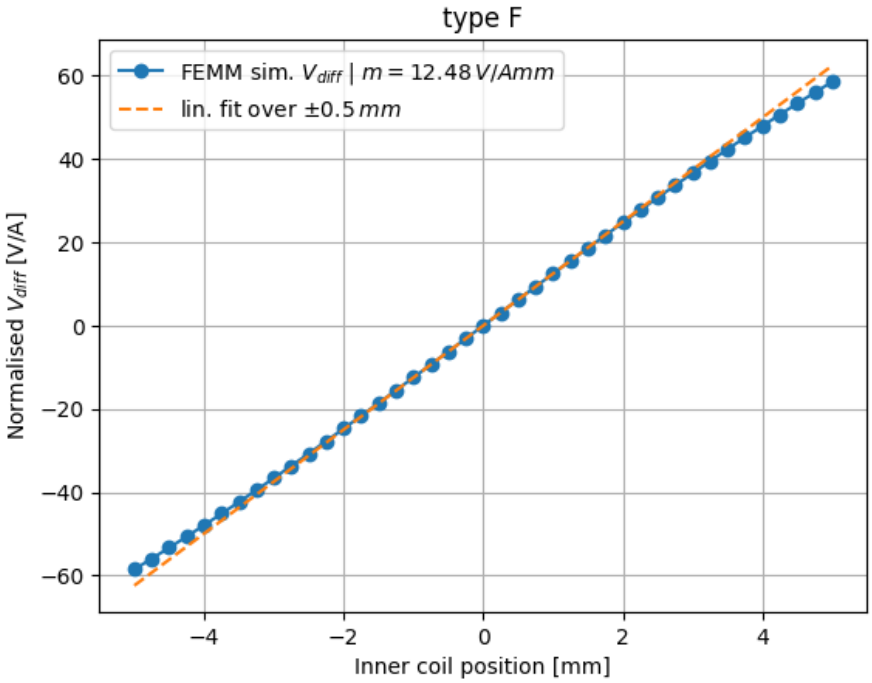

Fig. 3.3 FEMM simulated voltage difference V_{diff} and fitted linear curve for a type F LVDT for inner coil positions over $z = \pm 5\,mm$ with a stepsize of $0.25\,mm$. The linear fit is performed over a $z = \pm 0.5\,mm$ range.

The linear fit allows for the evaluation of the linearity of the V_{diff} by computing the normalised fit deviation D_f for the voltage:

$$D_f = |\frac{V_{diff,fit} - V_{diff,data}}{V_{diff,fit}}|. \tag{3.15}$$

Figure 3.4 shows the normalised fit deviation for the V_{diff} and linear fit shown in Fig. 3.3 for 2 fit ranges. The $z = 0\,mm$ position is omitted to avoid division by 0.

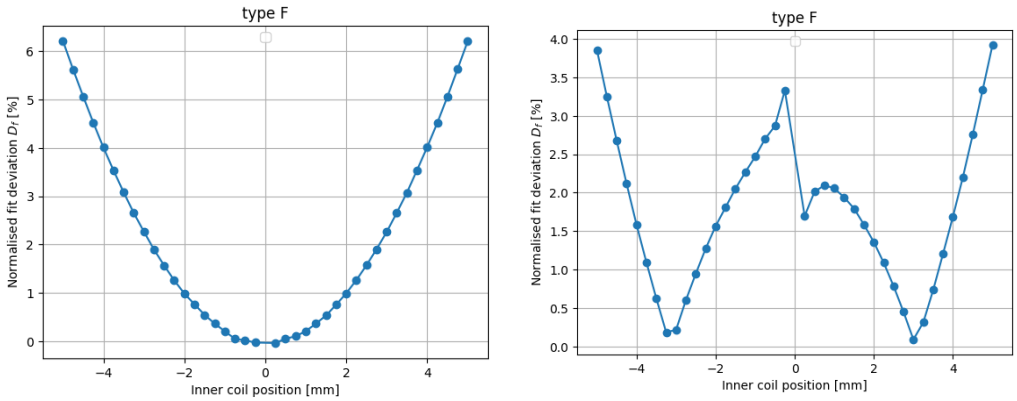

Fig. 3.4 Normalised fit deviation of V_{diff} for FEMM simulation of type F LVDT for inner coil positions over $z = \pm 5\,mm$ with a stepsize of $0.25\,mm$ omitting the $z = 0\,mm$ position. Left Panel: linear fit over a $z = \pm 0.5\,mm$ range. Right Panel: linear fit over a $z = \pm 4\,mm$ range.

The left panel of Figure 3.4 demonstrates that the simulated V_{diff} is most linear for an inner coil position near the center $z = 0\,mm$. Increasing the fit range increases the deviation near the central inner coil position and reduces the deviation for larger z, indicating the fit range to be too wide since LVDTs are designed to operate around the linear region of $z = 0\,mm$. The right panel of Fig. 3.4 illustrates the normalised fit deviation for an overly wide fit range. The simulation results of the type A LVDT are summarized in Figure 3.5.

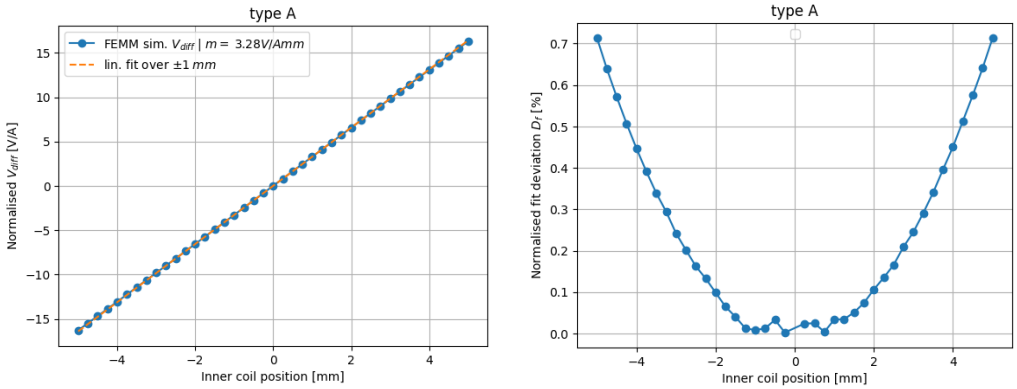

Fig. 3.5 FEMM simulated voltages for a type A LVDT for inner coil positions over $z = \pm 5\,mm$ with a stepsize of $0.25\,mm$. The linear fit is performed over a $z = \pm 1\,mm$ range. Left panel: voltage difference V_{diff}. Right panel: normalised fit deviation of V_{diff}, omitting the $z = 0\,mm$ position.

The discontinuous nature around $z \approx 0\,mm$ of the normalised fit deviation curve of the type A LVDT can be attributed to the division by small numbers and thus numerical instabilities. Comparing the two LVDT designs reveals type F to have a higher response; response type A $3.28\,V/Amm$ vs response type F: $12.48\,V/Amm$. Alternatively type A shows a larger linear region for V_{diff}; at $z = 5\,mm$ the normalised relative deviation of type A: $D_{f,A} \approx 0.7\%$ vs type F: $D_{f,F} \approx 6\%$.

3.3 Transversal inner coil movement

The effect of transversal movement of the inner coil on the response is analysed by investigating the $\mathbf{B}$ field inside the LVDT. For a given LVDT type one FEMM simulation is performed with the inner coil at the center position $z = 0\,mm$. Afterwards the $\mathbf{B}$ field vector at all positions of a coordinate grid can be extracted, allowing for the visualisation of the magnetic field, see Fig. 3.6. It should be noted that only the amplitude of the magnetic field is shown, since the field itself oscillates at the specified frequency $f = 10\,kHz$.

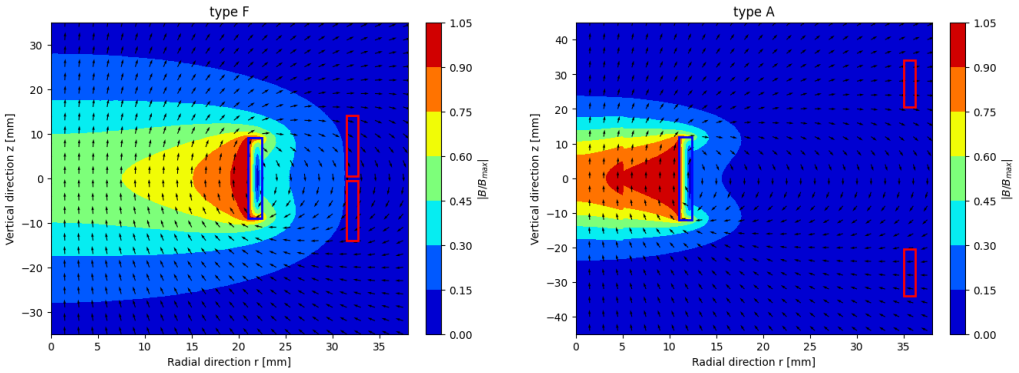

Fig. 3.6 FEMM simulated relative $\mathbf{B}$ field amplitude normalised to the highest $|\mathbf{B}|$ value for a central inner coil position $z = 0\,mm$. All vectors are normalised to the same length. The blue rectangle denotes the inner coil, the red rectangles the outer coils. Left panel: type F LVDT design. Right panel: type A LVDT design.

Transversal inner coil movement shifts the coils r coordinate. It is clear from the plotted fields that a change in r position will affect the magnetic field experienced by the outer coils. Since $\mathbf{B}$ is not invariant in the r direction, the induced voltage in the outer coils will be dependent on the inner coil's r coordinate. Moving the rectangle of the inner coil transversally in the r, z-plane in the simulation adjusts the inner coil's radius since FEMM addresses axisymmetric problems. To solve this problem a new hybrid method is developed to determine V_{diff} for an asymmetric inner coil position which uses both FEMM simulation and additional algorithms coded in *python*.

3.4 Asymmetric method

The new method is based on a numerical integration of the magnetic field eq. (2.3) from which the voltage induced in the coils is derived from the universal flux rule, i.e. eq. (2.2). The asymmetric scheme starts by performing an FEMM simulation with the inner coil in the central position $z = 0\,mm$ and extracting the magnetic field data on a grid similar to Fig. 3.6. The extracted magnetic field grid has a stepsize of $dr = 0.1$ for the radial direction and $dz = 0.01$ for the vertical direction. A transversal shift (r coordinate) of the inner coil is

imitated by shifting the integration area for Φ_B for the outer coils in the opposite direction. Figure 3.7 shows the top view of a horizontal cut of an axisymmetric B field (similar to the field generated by the inner coil) for symmetric and asymmetric outer coil positions, represented by the circles.

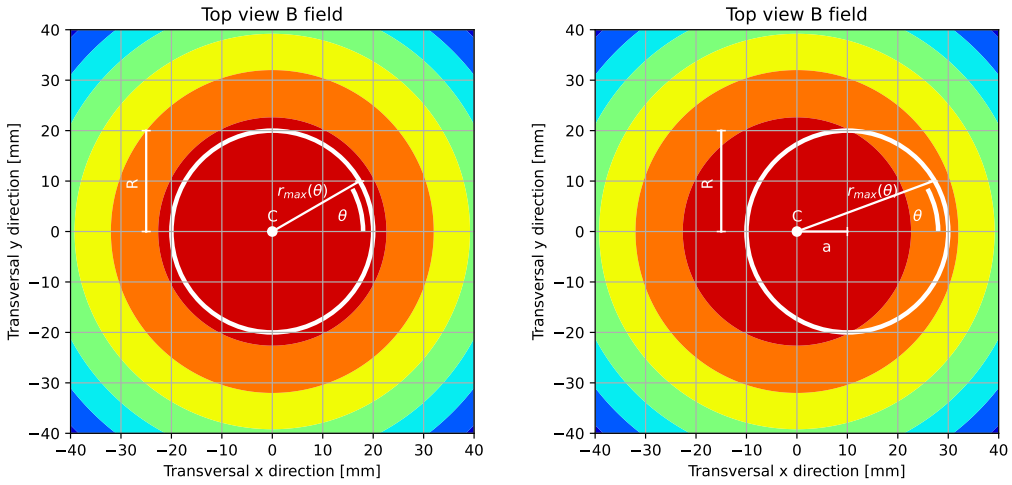

Fig. 3.7 Top view of a horizontal cut of an axisymmetric B field (similar to the field generated by the inner coil). The circles represent the position of the outer coils with radius R and B field center C. The transversal shift is denoted by a, the distance from the B field center C to the outer coil radius $r_{max}(\theta)$ is a function of angle θ. Left panel: symmetric outer coil position. Right panel: asymmetric outer coil position with transversal shift a.

The integral of eq. (2.3) is performed in the r, θ-plane (x, y-plane in polar coordinates) from the center of the magnetic field C to the edge of the outer coil $r_{max}(\theta)$. For a general asymmetric case where the outer coil is shifted by a distance a, the integration circle is also shifted. The integration area is shifted along the x-axis without loss of generality. Using the equation of the shifted circle the r_{max} dependency on θ is derived as follows:

$$\begin{aligned} (x-a)^2 + y^2 &= R^2 \\ (x^2+y^2) - 2ax &= R^2 - a^2 \end{aligned} \tag{3.16}$$

switching to polar coordinates

$$\begin{aligned} x &= r\cos(\theta) \\ y &= r\sin(\theta) \end{aligned}$$

and substituting the polar coordinates in (3.16) yields

$$\begin{aligned} & r^2 - 2ar\cos(\theta) + (a^2 - R^2) = 0 \\ \Rightarrow r = & \frac{2a\cos(\theta) \pm \sqrt{4a^2\cos^2(\theta) - 4(a^2 - R^2)}}{2} \\ = & a\cos(\theta) \pm \sqrt{a^2(\cos^2(\theta) - 1) + R^2} \\ = & a\cos(\theta) \pm \sqrt{R^2 - a^2\sin^2(\theta)}. \end{aligned} \tag{3.17}$$

The transversal shift a can not be larger than the outer coil radius R, i.e. $a \leq R$, this also rules out the lower $-$ solution of (3.17), such that the final form of $r_{max}(\theta)$ is found as:

$$r_{max}(\theta) = a\cos(\theta) + \sqrt{R^2 - a^2\sin^2(\theta)}. \tag{3.18}$$

Making use of (3.18), equation (2.3) can be computed:

$$\begin{aligned} \Phi_B(t) &= \int_\Sigma \mathbf{B}(r,t).d\mathbf{S} \\ &= \int_\Sigma B_z(r,t)dS \\ &= \int_0^{2\pi} d\theta \int_0^{r_{max}(\theta)} rB_z(r,t)dr \\ &= \int_0^{2\pi} d\theta \int_0^{r_{max}(\theta)} rsin(\omega t)B_z(r)dr \\ &= \underbrace{2\int_0^{\pi} d\theta \int_0^{r_{max}(\theta)} rB_z(r)dr}_{\Phi_B} sin(\omega t). \end{aligned} \tag{3.19}$$

The first step of (3.19) where $B_z(r,t)$ denotes the z component of $\mathbf{B}(r,t)$ is valid since $d\mathbf{S}$ is perpendicular to the r,θ-plane, i.e. pointing in the z direction, such that only the z component of the magnetic field contributes to generated emf in the coil. Furthermore the third step is a result of the oscillating magnetic field $B_z(r,t) = sin(\omega t)B_z(r)$. The last step makes use of the symmetry of the r, θ-plane, only requiring the integration of the upper half of the circle from Figure 3.7. Numerically Φ_B from (3.19) equates to integrating discrete vectors r and $B_z(r)$ extracted from the FEMM simulation (Fig. 3.6) with stepsize dr in terms of $rB_z(r)dr$ from 0 to an angular dependent upper boundary $r_{max}(\theta)$. This integral is performed for varying discrete values of θ with a stepsize $d\theta$ and afterwards integrating the result $2\int_0^{r_{max}(\theta)} rB_z(r)dr$ over θ itself.

This computation is performed at every discrete height of the z-axis throughout the LVDT system (Figure 3.6), resulting in a z dependent flux $\Phi_B(z)$. Equation (3.19) is rewritten as:

$$\Phi_B(z,t) = 2\int_0^{\pi} d\theta \int_0^{r_{max}(\theta)} rB_z(r,z)drsin(\omega t). \tag{3.20}$$

Figure 3.8 illustrates the concept of the integration of $\Phi_B(z)$ throughout the z-axis.

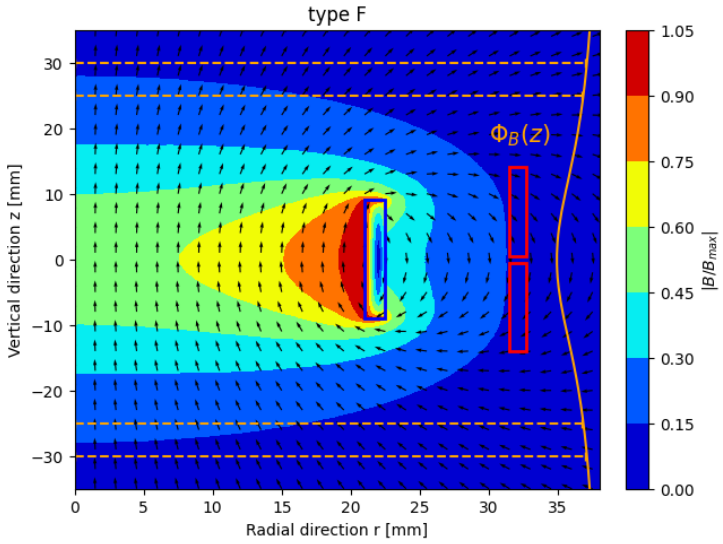

Fig. 3.8 Example of $\Phi_B(z)$, represented by the orange curve (eq. (3.20)), by integration of $\mathbf{B}(\mathbf{r}, \mathbf{z})$ in the r, θ-plane at every z position for a type F LVDT. The flux $\Phi_B(z)$ is not to scale and is only for illustrative purposes. The blue rectangle denotes the inner coil, the red rectangles the outer coils

From $\Phi_B(z)$ the induced voltage, which from this point will be referred to as V, in a single coil winding at a height z is reconstructed using eq. (2.2). Substituting $\Phi_B(z,t)$ into equation (2.2) yields:

$$\begin{aligned} V &= -\frac{d\Phi_B(z,t)}{dt} \\ &= -\Phi_B(z)\frac{d}{dt}\sin(\omega t) \\ &= -\omega\Phi_B(z)\cos(\omega t) \\ \Rightarrow V_{max} &= \omega\Phi_B(z) \end{aligned} \tag{3.21}$$

where V_{max} represents the amplitude of the induced voltage in a single coil winding. The flux is evaluated at every height z_i of the center of a coil wire and is summed to get the total induced voltage amplitude in an outer coil in 1 layer. Mathematically this equates to (3.22)

$$V_{coil,tot} = \omega \sum_{i=1}^{n} \Phi_B(z_i) \tag{3.22}$$

with n the number of turns per layer. Multiple coil layers of the outer coils are taken into account by computing $V_{coil,tot}$ for each coil layer. For each successive layer the integration area of eq.(3.20) increases due to a larger $r_{max}(\theta)$ for larger coil radii. The total outer coil

signal of a given outer coil: V_{upp}or V_{low} for all layers is the sum of the signals $V_{coil,tot,i}$ from eq.(3.22) (with *coil=upp* or *low*) of each individual layer, which equates to

$$V_{upp\ or\ low} = \sum_{i=1}^{l} V_{upp\ or\ low,tot,i} \tag{3.23}$$

with l the number of layers. A shift of the inner coil in the z direction is mimicked by shifting the outer coils in the opposite direction, represented in Fig. 3.9. Using equation (3.23) for varying shifts/positions of the z coordinate, the induced voltage in the upper and lower outer coils: V_{upp} and V_{low} are computed. From the outer coil voltages the voltage difference is derived $V_{diff} = V_{upp} - V_{low}$ similar to the axisymmetric FEMM simulation.

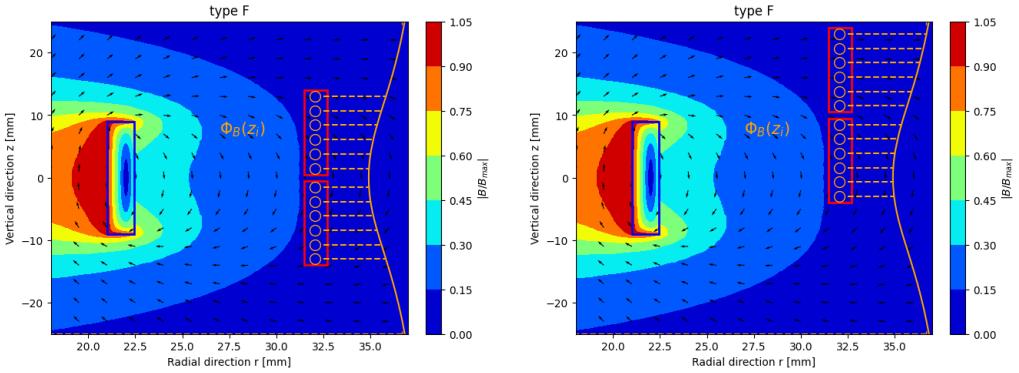

Fig. 3.9 Illustration of $V_{coil,tot}$ computation by evaluating $\Phi_B(z)$ at every z_i position of the center of a coil winding, illustrated by the orange circles. The orange curve represents $\Phi_B(z)$ (eq. (3.20)). The flux $\Phi_B(z)$ and number/size of the coil windings is not to scale and is only for illustrative purposes. The blue rectangle denotes the inner coil, the red rectangles the outer coils of a type F LVDT. Left panel: central position inner coil $z = 0\ mm$. Right panel: simulation of inner coil position shifted to $z = -10\ mm$ by shifting the outer coils with $z = 10\ mm$.

3.5 Asymmetric method compared to FEMM

The effect of adjusting the angular integration stepsize $d\theta$ from equation (3.19) is investigated by computing the flux $\Phi_B(z)$ for various values of $d\theta$ shown in Fig. 3.10.

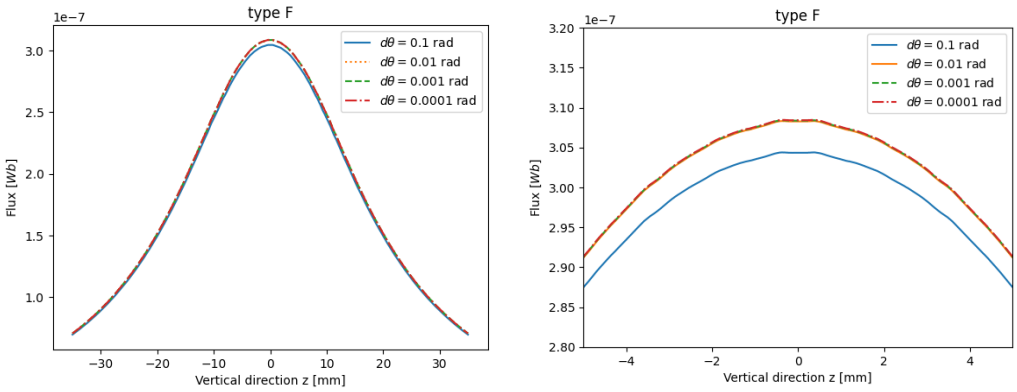

Fig. 3.10 Flux $\Phi_B(z)$ for a type F LVDT for different angular integration stepsizes $d\theta$. Left panel: $z = \pm 35\ mm$. Right panel: $z = \pm\ 5mm$.

Visually it is clear that for $d\theta = 0.01, 0.001, 0.0001\, rad$ the computation converges to a similar result. Qualitatively this is confirmed by deriving the relative deviation D_r of $\Phi_B(z)$ for $d\theta_i = 0.1, 0.01, 0.001\ rad$ compared to $\Phi_B(z)$ for $d\theta = 0.0001$:

$$D_r = \frac{\Phi_B(z)_{d\theta=0.0001} - \Phi_B(z)_{d\theta_i}}{\Phi_B(z)_{d\theta=0.0001}} \tag{3.24}$$

of which the result is shown in Fig. 3.11. The relative deviation of $d\theta = 0.1$ is not negligible at more than 1%. For the following simulations an angular stepsize of $d\theta = 0.01$ is chosen which strikes a balance between precision ($D_r < 0.05\%$) and computation speed. For type A a stepsize of $d\theta = 0.001$ is required to achieve a comparable precision due to larger outer coil radius of type A compared to type F.

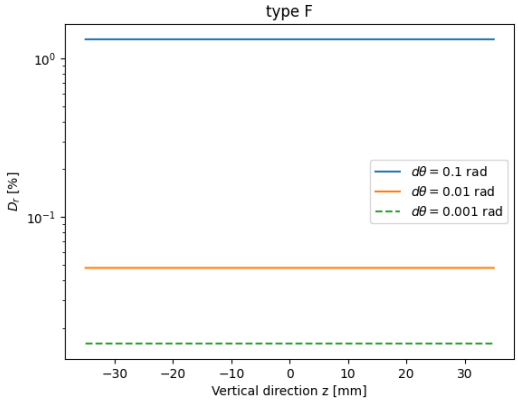

Fig. 3.11 Relative deviation D_r of $\Phi_B(z)$ for $d\theta_i = 0.1, 0.01, 0.001\ rad$ compared to $\Phi_B(z)$ for $d\theta = 0.1$. The flux is computed for a type F LVDT for $z = \pm 35\ mm$.

The new asymmetric method is validated by comparing the results to the axisymmetric FEMM simulations. By setting the transversal inner coil shift a for the asymmetric method to $a = 0\ mm$ the scheme also simulates an axisymmetric problem. The flux $\Phi_B(z)$ is extracted

from FEMM and compared to the flux $\Phi_B(z)$ using the asymmetric scheme in Figures 3.12 and 3.13 for type F and A respectively. The asymmetric method $\Phi_B(z)$ deviates no more than $\approx 0.9\%$ from the FEMM simulation $\Phi_B(z)$. The deviation between FEMM and the new method is attributed to numerical error; the magnetic field extracted from the initial FEMM simulation is saved on a grid with a given resolution: radial resolution $dr = 0.1$ and vertical resolution $dz = 0.01$. FEMM uses triangles and field smoothing techniques throughout the triangles interior leading to more precise results. Furthermore the asymmetric method integrates the magnetic field over the radial coordinate r and over the angle θ with stepsize $d\theta$. For the problems which FEMM addresses only a numerical integration over the radial coordinate is required due to the axial symmetry. The integration by the asymmetric method over the angle θ can thus introduce an extra numerical error.

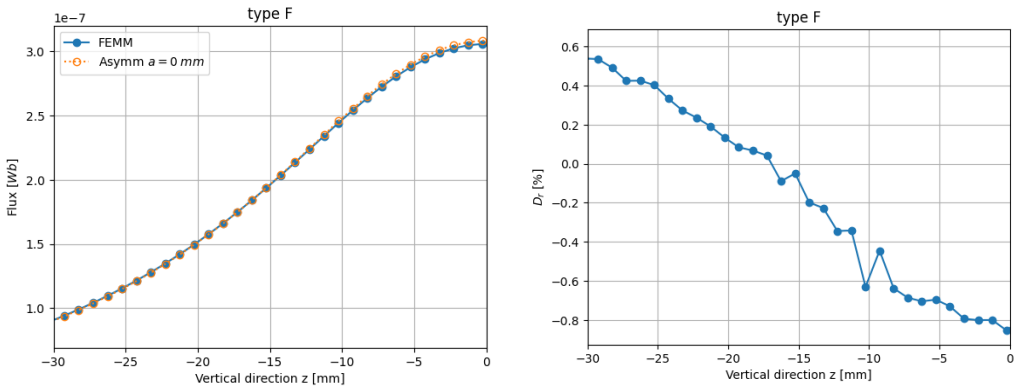

Fig. 3.12 Flux $\Phi_B(z)$ comparison between FEMM simulation and the asymmetric method for a type F LVDT. Only the $z = [-30, 0]\ mm$ region is shown with a stepsize of $1\ mm$, the flux is however symmetric over $z = 0\,mm$. Left panel: $\Phi_B(z)$ for FEMM and asymmetric method. Right panel: relative deviation of the asymmetric method compared to the FEMM simulation.

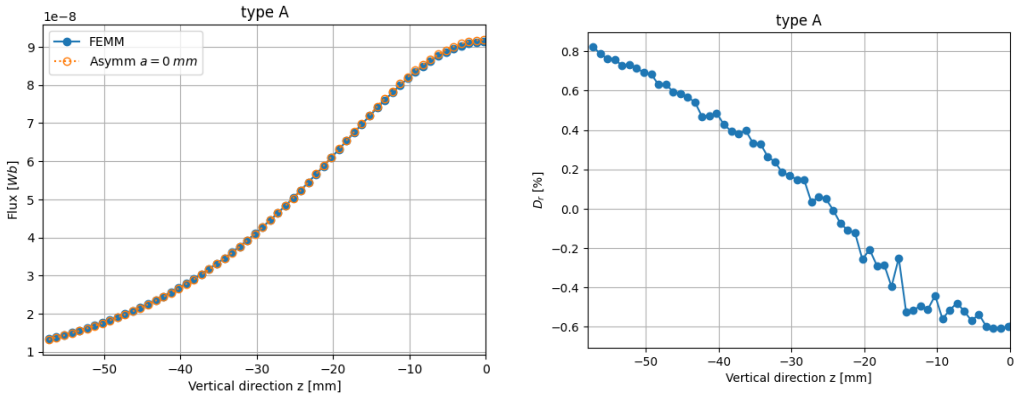

Fig. 3.13 Flux $\Phi_B(z)$ comparison between FEMM simulation and the asymmetric method for a type A LVDT. Only the $z = [-58, 0]\ mm$ region is shown with a stepsize of $1\ mm$, the flux is however symmetric over $z = 0\,mm$. Left panel: $\Phi_B(z)$ for FEMM and asymmetric method. Right panel: relative deviation of $\Phi_B(z)$ of the asymmetric method compared to the FEMM simulation.

However it is clear the asymmetric method for the symmetric case of $a = 0\,mm$ lines up with FEMM simulation, this is further supported by comparison of V_{diff} in Figures 3.14 and 3.15. The asymmetric method overshoots the absolute values of V_{diff} compared to FEMM. For type F the asymmetric scheme differs at most $\approx 0.8\,\%$ from the FEMM results, for type A this reduces to $\approx 0.18\,\%$. Table 3.1 summarizes the simulated responses. The response acquired from the asymmetric method deviates for both type F and A LVDT's no more than 1% from the FEMM response. Finally Fig. 3.16 shows the deviation of V_{diff} from the linear fit. The fit deviation of V_{diff} for the asymmetric method has a maximal absolute error of 0.2% compared to the FEMM fit deviation, which is the case for an inner coil position of $z = 5\,mm$ for type F (Left panel Fig. 3.16). The overlap of the results of the asymmetric method and the FEMM simulations shows the validity of the newly developed algorithms, therefore the asymmetric scheme will be used for non-axisymmetric systems with a transversal offset $a > 0\,mm$. The relative error on the fitted responses presented in Table 3.1 are overestimated to 0.8% and used as an error on the responses simulated by the asymmetric method for type F and A LVDTs.

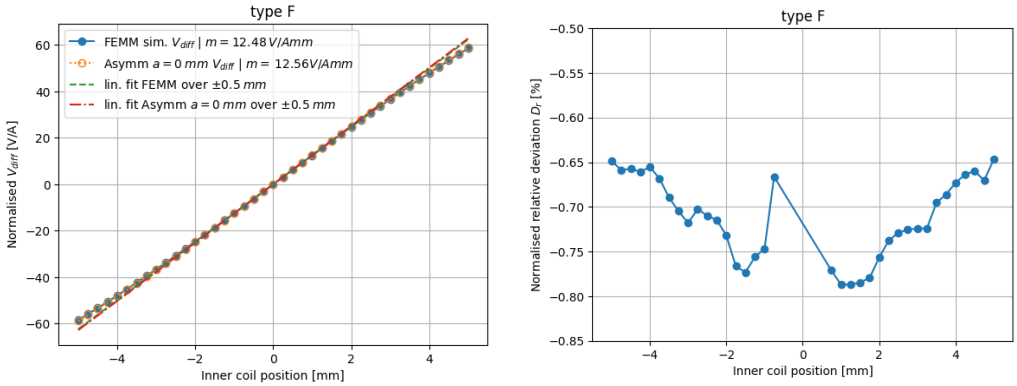

Fig. 3.14 Type F comparison FEMM and asymmetric simulation of V_{diff} for $z = \pm 5\,mm$ with a stepsize of $0.25\,mm$. Left panel: V_{diff} with a linear fit over $\pm\,0.5\,mm$. Right panel: normalised relative deviation D_f of V_{diff}.

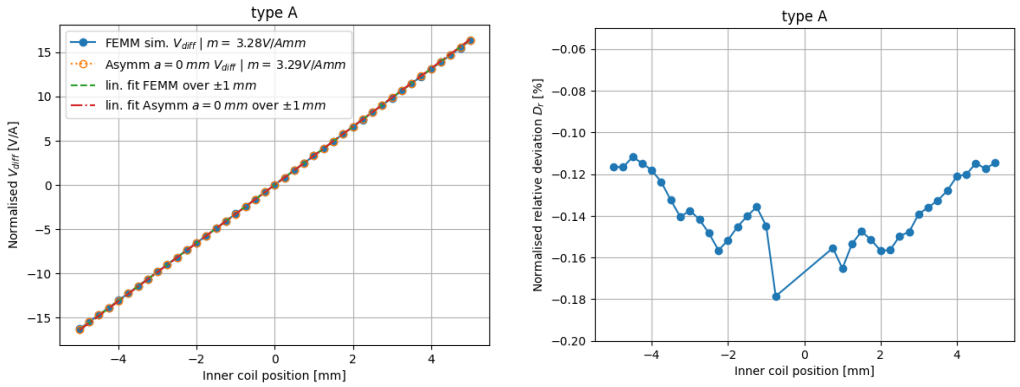

Fig. 3.15 Type A comparison FEMM and asymmetric simulation of V_{diff} for $z = \pm 5\,mm$ with a stepsize of $0.25\,mm$. Left panel: V_{diff} with a linear fit over $\pm\,1\,mm$. Right panel: normalised relative deviation D_f of V_{diff}.

LVDT	m FEMM $[V/Amm]$	m asymm $0\,mm$ $[V/Amm]$	dev. D_r [%]
Type F	12.48	12.57	0.7
Type A	3.28	3.29	0.3

Tab. 3.1 Response m for type F and type A LVDT's simulated by FEMM and the asymmetric method. D_r denotes the relative deviation of the asymmetric method compared to the FEMM simulation.

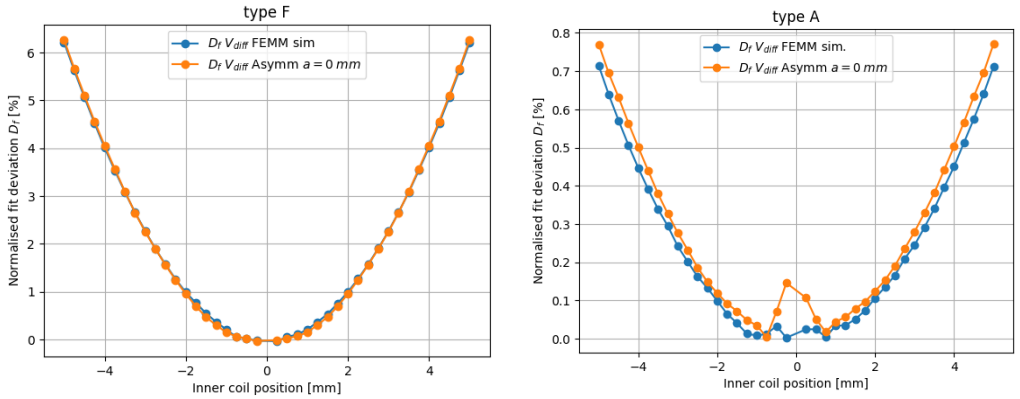

Fig. 3.16 Normalised fit deviation of V_{diff} for $z = \pm 5\,mm$ with a stepsize of $0.25\,mm$ for FEMM and asymmetric simulation, omitting the $z = 0\,mm$ data point. Left panel: type F with fit range $\pm\,0.5\,mm$. Right panel: type A with fit range $\pm\,1\,mm$

3.6 Asymmetric simulation results

The physical dimensions of the housing of the LVDT coils limit type F to a maximal transversal offset of $a = 6\,mm$. For type A an offset of $a = 19\,mm$ is practically achievable. The

evaluated transversal offsets a are chosen to maximize the probed region of the offset domain, while limiting the number of evaluation points. The range of offsets probed for type F: $a_F = [0, 1, 3, 5, 6]\ mm$ and for type A $a_A = [0, 1, 3, 5, 10, 15, 19]\ mm$. In section 4 the simulation will be compared to experimental measurement at the same evaluation points. Figure 3.17 shows the V_{diff} curves for varying transversal offsets for a type F LVDT.

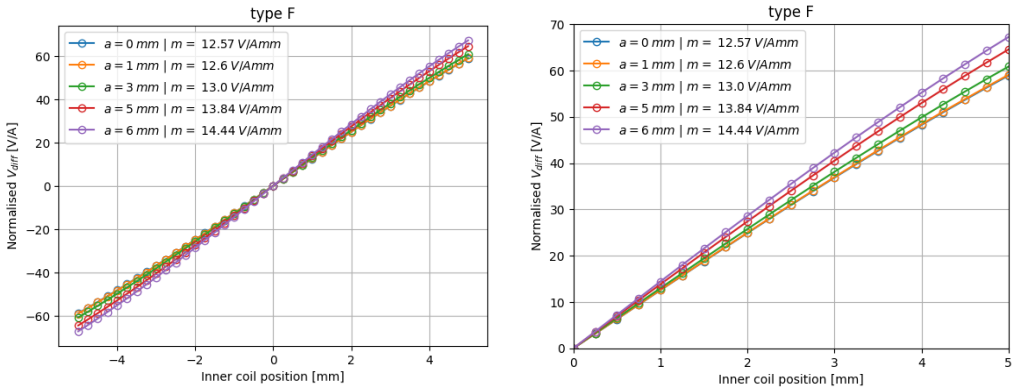

Fig. 3.17 Type F V_{diff} for varying transversal offsets a using the asymmetric method for $z = \pm 5\ mm$ with a stepsize of $0.25\ mm$. The responses are found by performing the linear fit over $z = \pm 0.5\ mm$ region. Left panel: full z height. Right panel: zoomed in on $z = [0, 5]\ mm$ region.

The asymmetric simulation predicts an increase in response for larger offsets a. The response shows an increase of $\approx 15\%$ for $a = 6\ mm$ compared to $a = 0\ mm$ for type F. The same tendency is found for type A in Fig. 3.18, which shows an increase of $\approx 6\%$ for $a = 19\ mm$ compared to $a = 0\ mm$. Along with an increase in response, the model also shows a less linear signal for larger offsets a, which is presented in the normalised relative fit deviation of V_{diff} in plots 3.19 and 3.20.

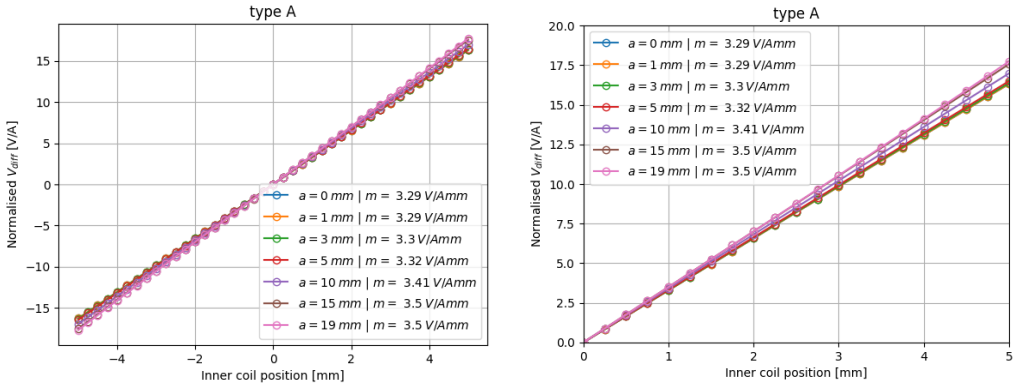

Fig. 3.18 Type A V_{diff} for varying transversal offsets a using the asymmetric method for $z = \pm 5\ mm$ with a stepsize of $0.25\ mm$. The responses are found by performing the linear fit over $z = \pm 1\ mm$ region. Left panel: full z height. Right panel: zoomed in on $z = [0, 5]\ mm$ region.

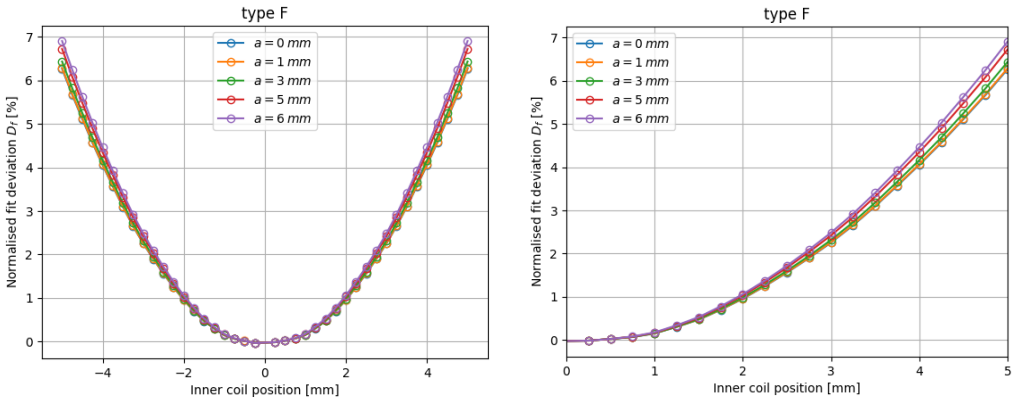

Fig. 3.19 Type F normalised fit deviation D_f of V_{diff} for varying transversal offsets a using the asymmetric method for $z = \pm 5\ mm$ with a stepsize of $0.25\ mm$. The linear fit has a range of $z = \pm 0.5\ mm$. Left panel: full z height. Right panel: zoomed in on $z = [0, 5]\ mm$ region.

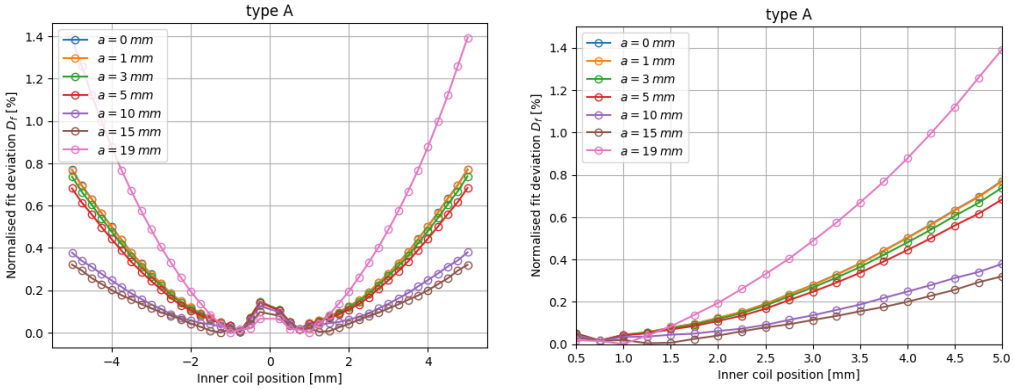

Fig. 3.20 Type A normalised fit deviation D_f of V_{diff} for varying transversal offsets a using the asymmetric method for $z = \pm 5\ mm$ with a stepsize of $0.25\ mm$. The linear fit has a range of $z = \pm 1\ mm$. Left panel: full z height. Right panel: zoomed in on $z = [0.5, 5]\ mm$ region.

For type A the normalised fit deviation decreases for $a = 0\ mm$ ($D_f(a = 0\ mm) \approx 0.8\,\%$) to $a = 15\ mm$ ($D_f(a = 0\ mm) \approx 0.3\,\%$) at $z = 5\ mm$, while increasing again to ($D_f(a = 0\ mm) \approx 1.4\,\%$) for $a = 19\ mm$. Omitting the absolute value in equation (3.15) yields a non absolute normalised fit deviation, which is presented in Figure 3.21. For $a = 0\ mm$ to $a = 10\ mm$ the V_{diff} data remains below the linear fit. For the offsets $a = 15\ mm$ and $a = 19mm$ the value of the data points at high z values exceeds the linear fit, indicated by the negative sign of D_f in Figure 3.21. The sign change of the fit deviation effectively improves the linearity compared to the symmetric inner coil position for offsets of $a = 1 - 15\ mm$.

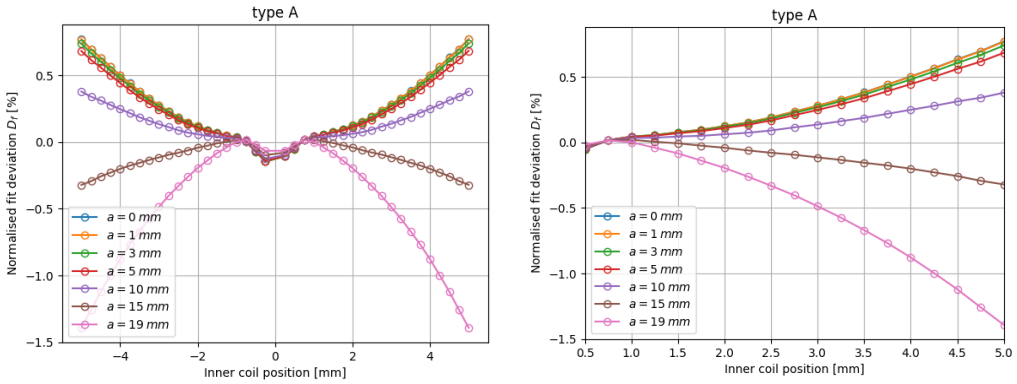

Fig. 3.21 Type A non absolute normalised fit deviation D_f of V_{diff} (eq. (3.15) without the absolute value) for varying transversal offsets a using the asymmetric method for $z = \pm 5\ mm$ with a stepsize of $0.25\ mm$. The linear fit has a range of $z = \pm 1\ mm$. Left panel: full z height. Right panel: zoomed in on $z = [0.5, 5]\ mm$ region.

The relative deviation D_r of the responses compared to the axisymmetric case $a = 0\ mm$ for each LVDT type is computed as

$$D_{r_a} = \frac{m_a - m_0}{m_0}. \tag{3.25}$$

Following [41] an error propagation on eq. (3.25) is performed as follows

$$\begin{aligned} \sigma_{D_{r_a}} &= \sqrt{\left(\frac{\partial D_{r_a}}{\partial m_0}\right)^2 \sigma_{m_0}^2 + \left(\frac{\partial D_{r_a}}{\partial m_a}\right)^2 \sigma_{m_a}^2} \\ &= \sqrt{\left(\frac{-m_a}{m_0^2}\right)^2 \sigma_{m_0}^2 + \left(\frac{1}{m_0}\right)^2 \sigma_{m_a}^2} \end{aligned} \tag{3.26}$$

The fitted responses with the corresponding relative deviation compared to the axisymmetric case $a = 0\,mm$ are shown in Tab. 3.2. Furthermore the error propagation is used to compute the respective error on the relative deviation, assuming the 0.8% error on the simulated responses resulting from the asymmetric method. The deviation allows for comparison with the experimental data in section 4. It should be noted that the σ_{D_r} values shown in the Tab. 3.2 represent an absolute error on D_r (which happens to have units of $\%$ itself). For clarification the relative error on D_r for type F at $a = 6\ mm$ is found as $D_r/\sigma_{D_r} = 1.4\,\%/14.9\,\% \approx 0.094$ equating to a relative error of $\approx 9.4\,\%$.

Type F | a	$0\,mm$	$1\,mm$	$3\,mm$	$5\,mm$	$6\,mm$		
$m\ [V/Amm]$	12.57	12.60	13.00	13.84	14.44		
$\sigma_m\ [V/Amm]$	0.11	0.11	0.11	0.12	0.12		
$D_r\ a = 0\ [\%]$	0	0.3	3.5	10.1	14.9		
$\sigma_{D_r}\ a = 0\ [\%]$	1.2	1.2	1.2	1.3	1.4		
Type A | a	$0\,mm$	$1\,mm$	$3\,mm$	$5\,mm$	$10\,mm$	$15\,mm$	$19\,mm$
$m\ [V/Amm]$	3.29	3.29	3.30	3.37	3.59	3.78	3.85
$\sigma_m\ [V/Amm]$	0.027	0.027	0.027	0.027	0.029	0.031	0.031
$D_r\ a = 0\ [\%]$	0	0	0.4	1.0	3.7	6.5	6.4
$\sigma_{D_r}\ a = 0\ [\%]$	1.2	1.2	1.2	1.2	1.2	1.3	1.3

Tab. 3.2 Response and relative deviation compared to $a = 0\,mm$ for type F and A LVDTs for varying transversal offsets a.

The relative deviation of the response for both type F and A are visualised in Figure 3.22. The relative change in response for type F increases more rapidly for a given offset a than for type A (type F $D_r(a = 3\,mm) = 3.5\%$ vs type A $D_r(a = 3\,mm) = 0.4\%$). Furthermore the maximal relative deviation of type F is higher than for type A (type F $D_r(a = 6\,mm) = 14.9\%$ vs type A $D_r(a = 15\,mm) = 6.5\%$). Type F is designed to operate in a smaller linear inner coil z range compared to type A as shown by the linear fit deviation plots (Figures 3.19 and 3.20). Additionally the dimensions of type A follow the LVDT relation $d = \sqrt{3}R$ more closely than type F, with d the outer coil distance and R the radius of the outer coils. Using the dimensions from Table 2.1:

$$\frac{d_F/R_F}{\sqrt{3}} \approx 0.27 < 0.90 \approx \frac{d_A/R_A}{\sqrt{3}}. \tag{3.27}$$

Equation (3.27) confirms the type A dimensions to be closer to the $d = \sqrt{3}R$ relation, therefore a larger relative deviation of type F compared to type A is expected. However the change in response may also be seen as a advantageous effect. The response is a measure for the induced electronic signal as a function of the vertical inner coil position change. Increasing the response by moving the inner coil position to a given offset a will effectively increase the vertical position resolution, however also increasing the deviation from linearity. (Fig. 3.19 and 3.20)

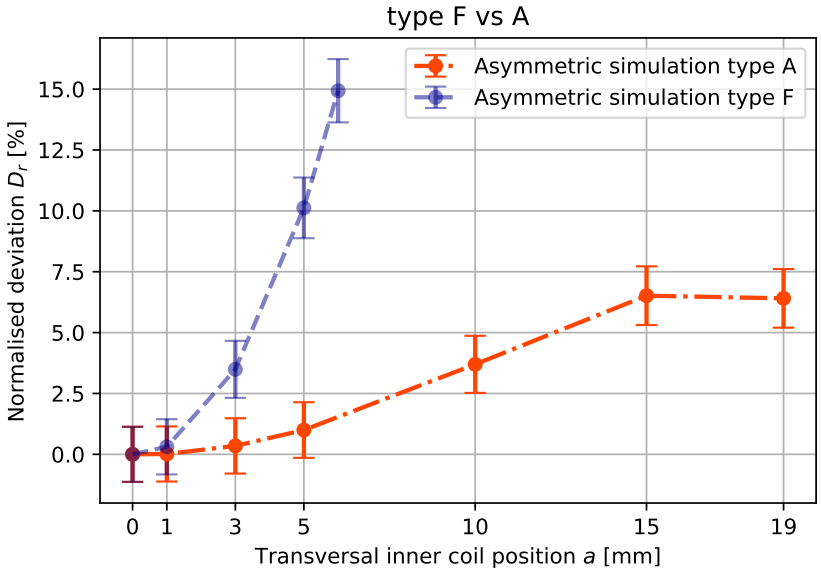

Fig. 3.22 Relative deviation of the response compared to the response in $a = 0\,mm$ for varying transversal offsets a. Type F response found by performing the linear fit over $z = \pm 0.5\,mm$ region, for type A over $z = \pm 1\,mm$.

Finally the effect of transversal movement for a constant vertical inner coil position z is plotted for type F and A in Figure 3.23. The plot shows the normalised outer coil signal V_{diff} changing as a function of the transversal offset a for a constant vertical inner coil position. A central inner coil position of $z = 0\,mm$ does not induce any differential voltage V_{diff} and is insensitive to transversal motion due to the symmetry between the upper and lower outer coils. Increasing the vertical inner coil position breaks the symmetry and increases the effect of transversal offsets on V_{diff}. For type F a maximal change in V_{diff} of $\approx 4\,V/A$ between $a = 0\,mm$ and $a = 6\,mm$ is observed for $z = 2\,mm$. For type A the maximal change in V_{diff} between $a = 0\,mm$ and $a = 19\,mm$ is found to be $\approx 0.5\,V/A$ at $z = 2\,mm$.

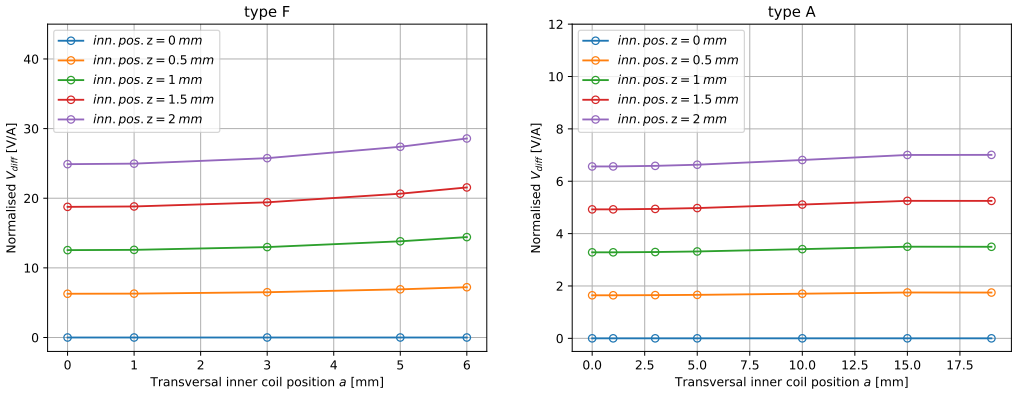

Fig. 3.23 Normalised V_{diff} in function of the transverse offset a for varying inner coil positions z. Left panel: type F. Right panel: type A.

An absolute value for the mimicked change in vertical inner coil position H_z as a function of transversal movement is found as

$$H_z(a) = \frac{V_{diff,z}(a) - V_{diff,z}(a = 0\,mm)}{m_{a=0\,mm}} \tag{3.28}$$

where the response for symmetric case $m_{a=0\,mm}$ is assumed. The $H_z(a)$ curves for type F and type A are presented in Figure 3.24. At $z = 2\,mm$ type F shows a maximal mimicked vertical displacement of $\approx 0.3\,mm$, for type A this is of the order of $\approx 0.14\,mm$. This implies moving the inner coil transversally to the edge of the operable range ($a = 6\,mm$ for type F, $a = 19\,mm$) at $z = 2\,mm$ appears as an additional vertical displacement to the control system of $\approx 2.3\,mm = 2\,mm + 0.3\,mm$ and $\approx 2.14\,mm = 2\,mm + 0.14\,mm$ for type F and A respectively.

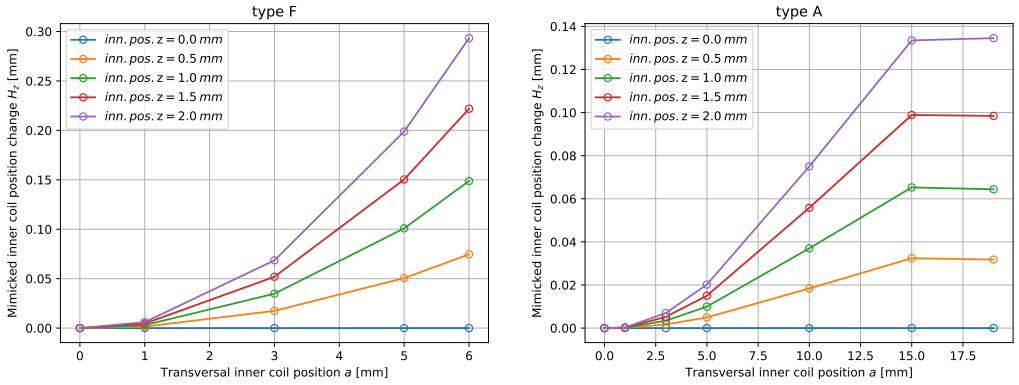

Fig. 3.24 The mimicked change in vertical inner coil position H_z as a function of the transversal offset a for varying inner coil positions z. Left panel: type F. Right panel: type A.

4 Experimental measurement

4.1 Test setup

Experimental measurements are carried out using a dedicated setup specifically designed for LVDT testing. The configuration of the system is described by referencing the components on Figure 4.1. The setup consists of a frame composed of metal profiles which houses an alignment table (A) to align the x, y position of the outer coil housing (O) to the inner coil housing (I). The table supports a structure (B) which holds the housing for the outer coils. The horizontal alignment of the outer coil housing can be adjusted by three vertical screws (S). A support bracket (C) (which can also be horizontally aligned with three adjustment screws) attached to the top of the metal frame holds vertical (V) and horizontal (H) PI stages, these are high precision actuators to control the position of the inner coil housing in the z and x direction respectively. While the outer coil housing remains stationary, the inner coil housing is connected to the stages via a vertical mounting arm (M). A laser position sensor (L) measures the vertical position z of the PI stage with outer coil housing, which can be positioned to its optimal sensing range by using a vertical actuator.

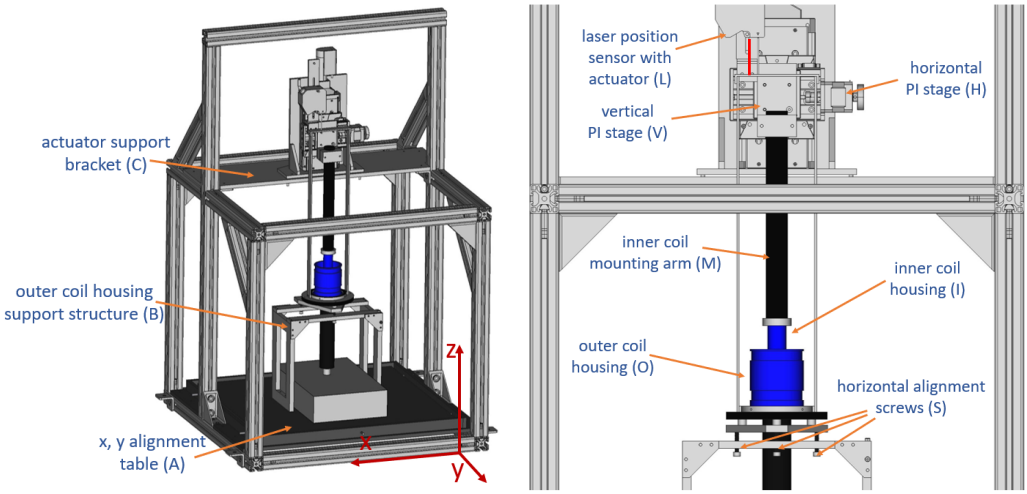

Fig. 4.1 Experimental test setup LVDT.

The type F LVDT is wound using a winding station in ETpathfinder, type A is wound at the Nikhef institute in Amsterdam. The outer coils are counter wound and connected in series such that the induced voltage in the outer coil wire is directly $V_{diff} = V_{upp} - V_{low}$. The coil housings are made from PEEK which has suitable outgassing properties [42] for the vacuum

conditions at ETpf. Since PEEK is a non-electrically conducting material no currents will be induced by any magnetic fields which could provide unwanted forces. The inner coil wire is connected to a DAC which controls the input signal, similarly the outer coil wire is connected to an amplification board. The inner coil is excited by a $10\,kHz$ oscillating voltage with an amplitude of $1\,V$. Contrary to FEMM the experimental voltage difference V_{diff} is normalised with an inner coil excitation voltage, i.e. V/V. FEMM requires an input current, however practically excitation is achieved by regulating the input voltage. The outer coil signal is amplified before being digitised by an ADC which samples the data at $100\,kHz$. The horizontal and vertical PI stages both have a resolution of $0.1\ \mu m$, the laser position sensor has a resolution of $0.001\ \mu m$. The electronic noise of the system for the voltage readout is estimated to be $\approx\ 1.8 * 10^{-6}\ V/\sqrt{Hz}$ at $10\ kHz$.

4.2 Measurement and data analysis

The vertical PI stage allows for vertical movement on the z axis of the inner coil housing, horizontal transversal movement a is provided by the horizontal PI stage. The laser position sensor is used as an additional precise vertical position reference. For each measurement the transversal offset a is set by actuating the stepper to the corresponding horizontal position. The vertical z direction is probed by setting the inner coil position to a given height and recording the voltage difference signal V_{diff} in the outer coils with a duration of $1\ s$. This measurement duration should provide sufficient time to gather ample data points while also limiting low frequency environmental effects. A sweep of inner coil positions z for a given offset a constitutes one measurement set. Measurement sets are performed for the same transversal offsets as in the simulations, see Tab. 3.2. Furthermore since the experimental setup allows the inner coil to move in the entire r,z-plane, offsets to the left $a \leq 0\ mm$ and to the right $a \geq 0\ mm$ of the horizontal axisymmetric center $z = 0\ mm$ are achievable. Figure 4.2 shows photo's of the dedicated setup, the left panel shows a type F LVDT with a transverse offset to the left.

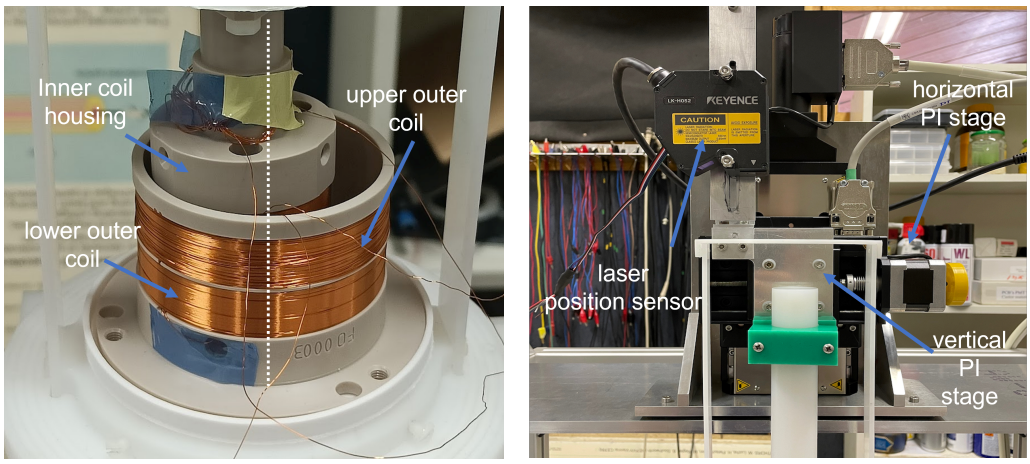

Fig. 4.2 Pictures of the experimental setup. Left panel: type F LVDT with an inner coil housing shifted $a = 5\,mm$ to the left of the outer coil housing center. Right panel: actuators and sensors mounted to the support bracket.

6 measurement sets are taken for type F. The first 4 sets (M1F left, M1F right, M2F left, M2F right) for inner coil positions of $z = \pm 2.5\,mm$ with a stepsize of $0.25\,mm$ with transverse displacements a to the left and right; The last 2 sets (M3F left, M3F right) for inner coil positions of $z = \pm 1\,mm$ with a stepsize of $0.1\,mm$. For type A 4 sets are performed (M1A left, M1A right, M2A left, M2A right) for inner coil positions over $z = \pm 2.5\,mm$ with a stepsize of $0.25\,mm$. All measurement parameters are summarized in Tab. 4.1.

Type F set	$z\ [mm]$	step $[mm]$	a	Type A set	$z\ [mm]$	step $[mm]$	a
M1F left	± 2.5	± 0.25	≤ 0	M1A left	± 2.5	± 0.25	≤ 0
M1F right	± 2.5	± 0.25	≥ 0	M1A right	± 2.5	± 0.25	≥ 0
M2F left	± 2.5	± 0.25	≤ 0	M2A left	± 2.5	± 0.25	≤ 0
M2F right	± 2.5	± 0.25	≥ 0	M2A right	± 2.5	± 0.25	≥ 0
M3F left	± 1	± 0.1	≤ 0				
M3F right	± 1	± 0.1	≥ 0				

Tab. 4.1 Parameters measurement sets. The probed inner coil position range is denoted by z, the stepsize by step. The parameter a shows if the measurement set is performed for transverse offsets to the left $a \leq 0$ or to the right $a \geq 0$, as shown in the left panel of Figure 4.2.

The sampled data $V(t)$ from the outer coil signal for each measurement is analysed by curve fitting a sine function $f(t)$ on the data:

$$f(t) = Asin(\omega t + \phi) + c \tag{4.1}$$

with amplitude A, angular frequency ω, phase offset ϕ and constant offset c. To achieve a successful curve fit of the sampled data, the parameters A, ω and c require a suitable initial

guess value. The parameter guess value for the amplitude A_{guess} is based on the standard deviation σ:

$$A_{guess} = 2 * \sigma_{V(t)}. \tag{4.2}$$

The angular frequency ω_{guess} is estimated by a Fast Fourier Transform (FFT) of the data in equation (4.3)(the FFT provides an additional check on the data, in actuality the guess can be set as $\omega_{guess} = 2 * \pi * 10\ kHz$).

$$\omega_{guess} = 2 * \pi * FFT(V(t)). \tag{4.3}$$

Finally the constant offset c_{guess} is derived by averaging the data:

$$c_{guess} = \overline{V(t)}. \tag{4.4}$$

Fitting eq. (4.1) on the data $V(t)$ yields the induced voltage difference as the amplitude $A = V_{diff}$. From the analysed values of V_{diff} and the laser sensor data for the vertical inner coil position, the voltage difference curves are reconstructed in Figure 4.3 for both type F and type A. No error bars on the voltage difference and inner coil position (z and a) are shown for clearer visualisation of the data. Furthermore the magnitude of the environmental noise (inner coil position drift, vibrations, ...) on the data outweighs the z position resolution of $0.001\ \mu m$, offset a resolution of $0.1\ \mu m$ and noise on the voltage of $\approx\ 1.8 * 10^{-6}\ V/\sqrt{Hz}$ at $10\ kHz$. The effective error on the data is later on determined by computing the standard deviation of the measurement sets.

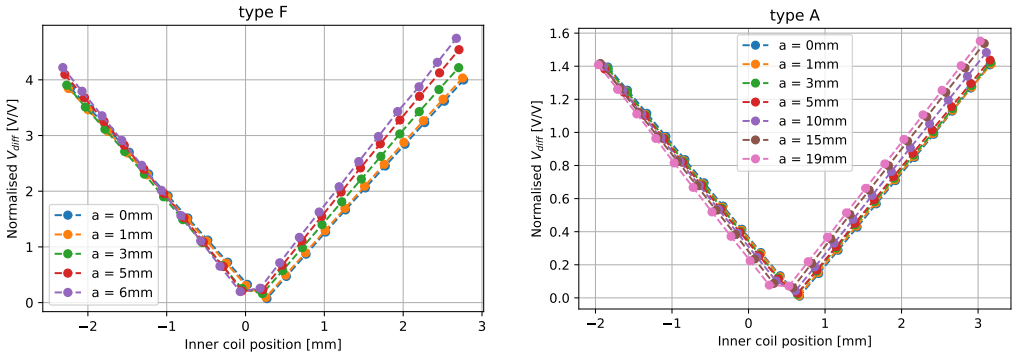

Fig. 4.3 Normalised V_{diff} for inner coil positions over $z = \pm\ 2.5\ mm$ with a stepsize of $0.25\ mm$. Left panel: type F measurement set M1F left. Right panel: type A measurement set M1A left.

Figure 4.3 shows a positive V_{diff} for both positive and negative inner coil positions. While transitioning from negative to positive inner coil positions the phase of V_{diff} switches which results in the sign change of V_{diff} visible in Figure 3.3. The experimental data collected from the outer coil signal does not take the phase of V_{diff} into account. As there is currently no reference phase to compare to. Therefore V_{diff} is mirrored manually over the x-axis: inner coil position axis, for all data points of Fig. 4.3 left from the minimal V_{diff} value. Examples are shown in Figures 4.4, 4.5 and 4.6

The inner coil positions for the varying offsets a don't align even though identical vertical actuator positions are specified. Environmental factors such as temperature fluctuations, vibrations, imprecise actuator movements, ... cause a drift on the inner coil positions which shift the vertical center of the inner coil. For this reason the vertical position is measured by the laser sensor and chosen as a reference. The drift prohibits a direct comparison of the V_{diff} values for a given vertical inner coil position, however the normalised fitted response is insensitive to a shift of the data points, provided the shift is sufficiently small such that the data points remain in the linear region.

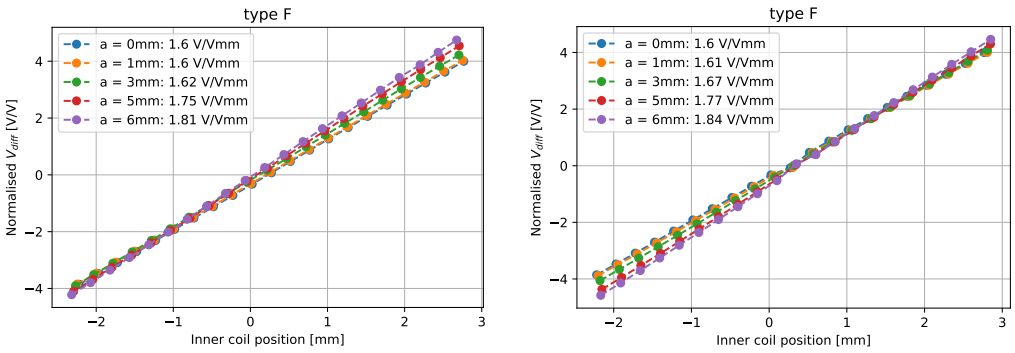

Fig. 4.4 Normalised V_{diff} with phase shift correction for a type F LVDT. The shown responses are fitted in the $z = \pm 0.5\,mm$ region. Left panel: M1F left set. Right panel: M1F right set.

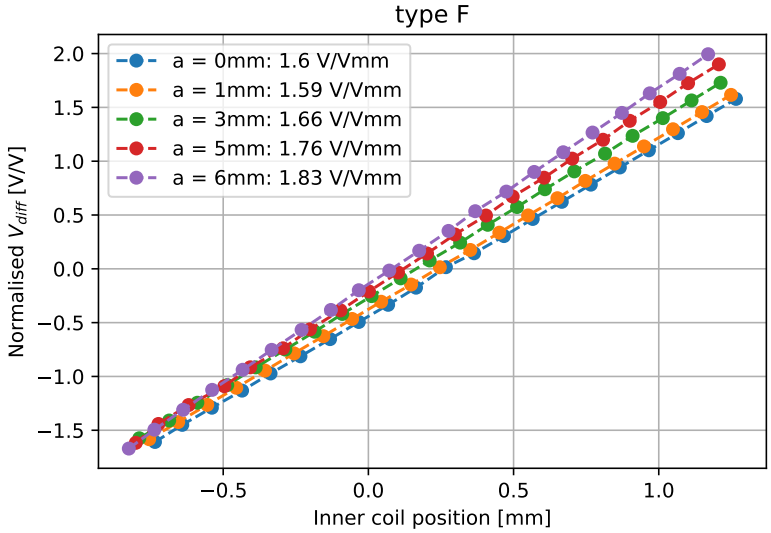

Fig. 4.5 Normalised V_{diff} with phase shift correction for a type F LVDT for measurement set M3F left. The shown responses are fitted in the $z = \pm 0.5\,mm$ region.

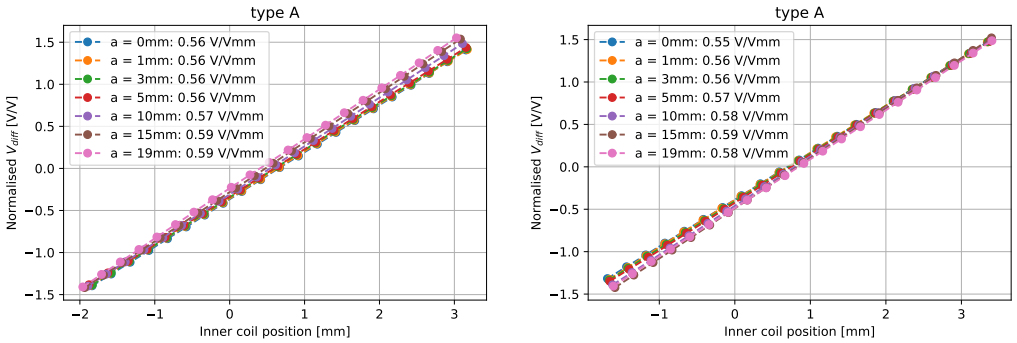

Fig. 4.6 Normalised V_{diff} with phase shift correction for a type A LVDT. The shown responses are fitted in the $z = \pm\, 1\ mm$ region. Left panel: M1A left set. Right panel: M2A right set.

Tables 4.2 and 4.3 show the fitted response of the measurement sets for type F and type A respectively. Comparing the measurement sets for a given LVDT design shows no systematic difference in response between transversal offsets to the left and right. A general increase in response as a function of the transverse displacement is visible in the data. However the response for a given offset a does noticeably fluctuate. Therefore a proper analysis of the data is required to establish any conclusive trends.

Type F | a	$0\ mm$	$1\ mm$	$3\ mm$	$5\ mm$	$6\ mm$
m M1F left $[V/Vmm]$	1.604	1.596	1.621	1.751	1.814
m M1F right $[V/Vmm]$	1.604	1.606	1.667	1.766	1.841
m M2F left $[V/Vmm]$	1.600	1.599	1.660	1.761	1.814
m M2F right $[V/Vmm]$	1.600	1.597	1.657	1.774	1.837
m M3F left $[V/Vmm]$	1.597	1.592	1.662	1.757	1.827
m M3F right $[V/Vmm]$	1.597	1.596	1.658	1.776	1.852

Tab. 4.2 Response m for the measurement sets M1F, M2F and M3F (left and right) of type F LVDT for varying transversal offsets a fitted over $z = \pm\, 0.5\ mm$. For $a = 0\ mm$ (the center position) measurement is incorporated in both left and right measurement set. (M1F left($a = 0\ mm$) = M1F right($a = 0\ mm$) similar for M2F and M3F.)

Type A | a	$0\ mm$	$1\ mm$	$3\ mm$	$5\ mm$	$10\ mm$	$15\ mm$	$19\ mm$
m M1A left $[V/Vmm]$	0.560	0.561	0.563	0.563	0.574	0.591	0.587
m M1A right $[V/Vmm]$	0.560	0.557	0.562	0.567	0.580	0.588	0.581
m M2A left $[V/Vmm]$	0.557	0.561	0.562	0.563	0.573	0.586	0.587
m M2A right $[V/Vmm]$	0.553	0.558	0.563	0.567	0.581	0.591	0.575

Tab. 4.3 Response m for the measurement sets M1A and M2A (left and right) of type A LVDT for varying transversal offsets a fitted over $z = \pm\, 1\ mm$.

For each transversal offset a the average of the responses $\overline{m_a}$ of all measurement sets is computed, and the standard deviation on the responses is found as:

$$\sigma_{m_a} = \sqrt{\frac{\sum_{i=1}^{n}(m_{i_a} - \overline{m_a})^2}{n}} \tag{4.5}$$

with i looping over the measurement sets: (M1F left, M1F right, M2F left, ...) for each LVDT design. It should be noted that for type F for $a = 0\,mm$ the number of measurements is half of the number for $|a| > 0\,mm$, since for $a = 0\,mm$ the same measurement is incorporated in both the left and right sets. The average responses with corresponding standard deviations are presented in Table 4.4 for type F and Table 4.5 for type A.

Type F | a	$0\,mm$	$1\,mm$	$3\,mm$	$5\,mm$	$6\,mm$
m avg. $[V/Vmm]$	1.6001	1.5976	1.654	1.7653	1.831
σ_m $[V/Vmm]$	0.0029	0.0045	0.016	0.0079	0.015

Tab. 4.4 Average response m and deviation σ_m for the measurement sets M1, M2 and M3 (left and right) of type F for varying transversal offsets a.

Type A | a	$0\,mm$	$1\,mm$	$3\,mm$	$5\,mm$	$10\,mm$	$15\,mm$	$19\,mm$
m avg. $[V/Vmm]$	0.5575	0.5592	0.56254	0.5649	0.5770	0.5892	0.5827
m σ_m $[V/Vmm]$	0.0029	0.0019	0.00052	0.0022	0.0037	0.0022	0.0050

Tab. 4.5 Average response m and deviation σ_m for the measurement sets M1 and M2 (left and right) of type A for varying transversal offsets a.

The drift on the test setup's inner coil position and noise on the data prohibits a clear comparison of the simulated and experimental normalised linear fit deviation D_f, derived in equation (3.15). Figure 4.7 shows an example of D_f for measurements of type F and type A LVDTs. The fluctuation of the measured D_f prevents any conclusive verification of the simulated curves in Figures 3.19 and 3.20. Similarly the simulated mimicked height change H_z derived in equation (3.28) is not compared to the experimental data.

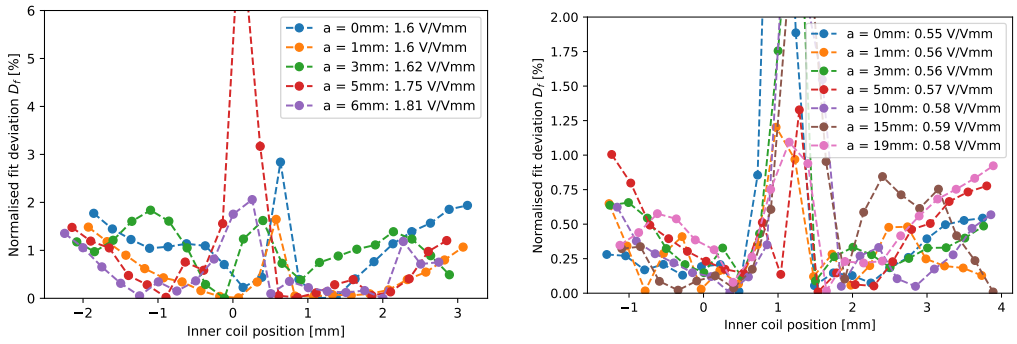

Fig. 4.7 Normalised fit deviation of V_{diff} for varying transversal offsets a. Left panel: type F measurement set M1F left for a linear fit over $z = \pm 0.5\,mm$. Right panel: type A measurement set M2A right for a linear fit over $z = \pm 1\,mm$.

It is however possible to compare the simulated (sim.) and measured (exp.) response by making a conversion between $m_{sim.}$ in units of V/Amm to $m_{exp.}$ in units of V/Vmm. Taking all necessary correction factors (amplification board gain, impedance, and current to voltage source conversion) into account yields a conversion factor of $c \approx 0.1177\, A/V$. Converting the type F $a = 0\, mm$ response from Table 3.2 results in $m_{sim.} = 1.479 \pm 0.012\, V/Vmm$ which underestimates the experimental value of $1.6001 \pm 0.0029\, V/Vmm$ (from Table 4.4) by $\approx 8\,\%$. The simulation is reasonably close to the experimental data, and is expected to be caused by imperfect winding of the coil. To avoid this uncertainty on calibration we do however continue with relative measurements.

The relative deviation D_r of the responses at varying offsets a compared to the axisymmetric case $a = 0\, mm$ is computed using eq. (3.25). The error is propagated similarly to the simulation results, i.e. equation (3.26). Tables 4.6 and 4.7 show a comparison of the simulated (Tab. 3.2) and measured relative deviation for type F and A respectively.

a| Type F	D_r sim. $a = 0\, mm$	D_r exp. $a = 0\, mm$
$0\, mm$	0 ± 1.2	0 ± 0.26
$1\, mm$	0.3 ± 1.2	-0.16 ± 0.33
$3\, mm$	3.5 ± 1.2	3.37 ± 0.98
$5\, mm$	10.1 ± 1.3	10.32 ± 0.53
$6\, mm$	14.9 ± 1.4	14.40 ± 0.91

Tab. 4.6 Simulated (sim.) and average measured (exp.) relative response deviation D_r from the measurement sets M1, M2 and M3 of type F LVDT for varying transversal offsets a to the left and right.

a| Type A	D_r sim. $a = 0\, mm$	D_r exp. $a = 0\, mm$
$0\, mm$	0 ± 1.2	0 ± 0.73
$1\, mm$	0 ± 1.2	0.31 ± 0.61
$3\, mm$	0.4 ± 1.2	0.91 ± 0.53
$5\, mm$	1.0 ± 1.2	1.34 ± 0.65
$10\, mm$	3.7 ± 1.2	3.50 ± 0.85
$15\, mm$	6.5 ± 1.3	5.69 ± 0.67
$19\, mm$	6.4 ± 1.3	4.5 ± 1.1

Tab. 4.7 Simulated (sim.) and average measured (exp.) relative response deviation D_r from the measurement sets M1 and M2 of type A LVDT for varying transversal offsets a to the left and right.

Figures 4.8 and 4.9 present the data from Tables 4.6 and 4.7 respectively, in terms of D_r as a function of transversal offset a. The measurements align with the simulated results within the uncertainties. Omitting the overestimated uncertainty of 0.8% assigned to the simulated responses and corresponding uncertainty on the relative response deviation D_r; the simulation results show a similar trend as the experimental results. For type F only at $a = 1\, mm$ does the simulated D_r^F lay outside the experimental 1σ error bar ($D_r^F(a = 1\, mm) = 0.3\%$). For type A the simulated D_r^A for $a = 15\, mm$ ($D_r^A(a = 15\, mm) = 6.5\%$) and for $a = 19\, mm$ ($D_r^A(a = 19\, mm) = 6.4\%$) are outside the 1σ experimental uncertainty. The drift of the inner coil position, vibrations of the setup, electrical noise in the excitation

and amplification electronics as well as imperfectly wound coils introduce noise to the measurement. However all simulated D_r without the assigned uncertainty overlap with a 2σ experimental uncertainty. The measurements confirm the developed simulation method and proves the schemes predictive power. The effect of transversal motion is experimentally observable and may hamper the LVDTs position inner coil position measurement if proper care is not taken.

Additionally, the agreeing simulation and experimental results for D_r leads one to expect the simulated mimicked z movement by transverse motion as shown in Figure 3.24 to similarly agree with experiment, assuming the LVDT to be perfectly wound. Minimising the drift on the inner coil position may allow for an experimental validation of this effect.

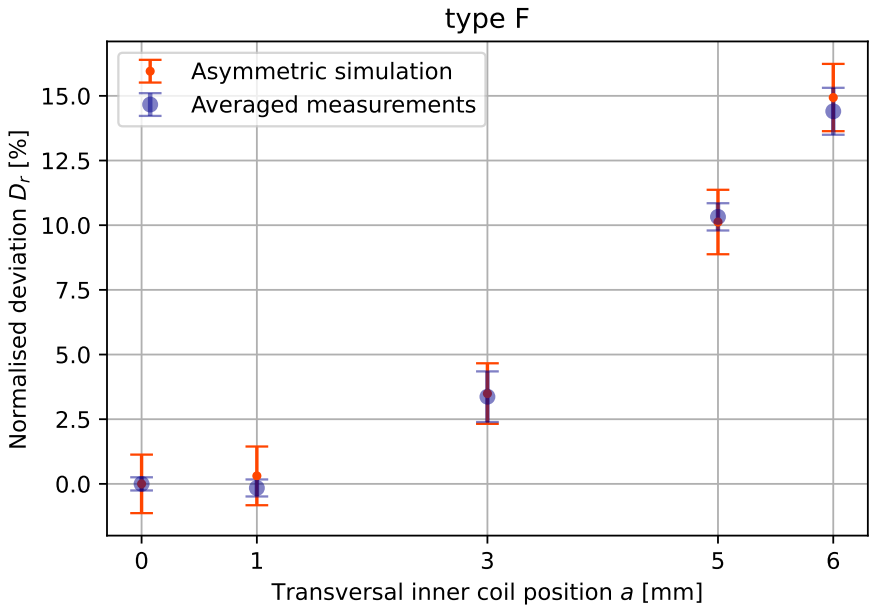

Fig. 4.8 Type F relative response deviation compared to the response in $a = 0\,mm$ for varying transversal offsets a, derived from the asymmetric simulation method and experimental measurements. The Response found by performing the linear fit over $z = \pm 0.5\,mm$ region.

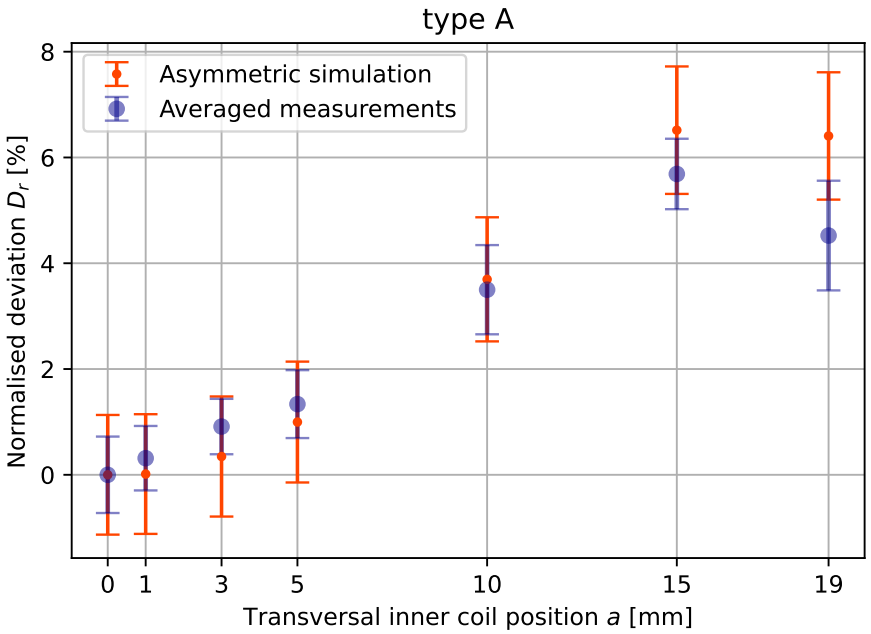

Fig. 4.9 Type A relative response deviation compared to the response in $a = 0\,mm$ for varying transversal offsets a, derived from the asymmetric simulation method and experimental measurements. The Response found by performing the linear fit over $z = \pm 1\,mm$ region.

5 Conclusion

The first direct gravitational wave observation in 2015 announced the beginning of a new age of astronomy. Although numerous GWs have been observed to date, a new generation of detectors of vastly enhanced sensitivity will increase detections into potentially an hourly occurrence, unlocking the full potential of the GW science domain. The Einstein Telescope is the European GW detector which promises to usher observations into a new era. For ET to reach the desired sensitivity, R&D of new and improved technologies is essential. ETpathfinder is a proof of concept experiment for this specific purpose. One of the major limiting factors of GW detectors is environmental noise. Therefore passive and active seismic attenuation systems are crucial. These consist of various pendulum stages fitted with sensors and actuators to actively control the mirror suspension. The Linear Variable Differential Transformer is a position sensor which generates a highly linear signal as a function of the measured displacement, and is widely used in ETpf. Furthermore the sensor is assumed to be insensitive to transverse motion.

This assumption is tested by simulating and experimentally measuring the response of the ETpf type F and type A LVDTs for varying transversal offsets a. To account for the transversal offsets, a simulation is developed which starts from a finite element method (FEMM) axisymmetric simulation of the LVDTs. The data extracted from the axisymmetric simulation is used for numerical algorithms which mimic the effect of transversal motion.

The simulation predicts an increase in LVDT response for increasing transversal offset a, agreeing with experimental measurement. The results confirm that the optimal operating volume of the inner coil is constrained to a small portion of the available transversal space. For a type F LVDT, transversal offsets of $a = 3\,mm$ induce a relative response deviation of $3.37 \pm 0.98\,\%$, this increases to $14.40 \pm 0.91\,\%$ for an offset $a = 6\,mm$. The response for a type A LVDT is less dependent on the offset; at $a = 3\,mm$ the relative deviation approaches $0.91 \pm 0.53\,\%$, the maximal relative deviation of $5.69 \pm 0.67\,\%$ is induced for a larger offset of $a = 15\,mm$.

Additionally the linearity of the differential outer coil signal decreases for increasing offsets a for type F. For type F the normalised relative deviation from a linear fit increases from $\approx\ 6.2\,\%$ at $a = 0\,mm$ to $\approx\ 7\,\%$ at $a = 6\,mm$ at an inner coil position of $z = 5\,mm$. A larger relative change in the linearity is simulated for type A, at an inner coil position of $z = 5\,mm$ the symmetric case $a = 0\,mm$ shows a deviation from linearity of $\approx\ 0.8\,\%$, for offsets between $a = 1\ -\ 15\,mm$, this lowers to a minimum at $a = 15\,mm$ of $\approx\ 0.3\,\%$ and afterwards raises at the edge $a = 19\,mm$ to $\approx\ 1.4\,\%$. However an experimental assessment of the normalised linear fit deviation shows inconclusive results due to fluctuating data. A drift on the position of the inner coil position in the test setup as well as additional noise

due to environmental factors prevent an absolute comparison of the differential outer coil signal V_{diff} between measurements at different offsets a. The response corresponds to the slope of the voltage difference V_{diff} as a function of the inner coil position z and is thus inherently less effected by a shift of the data points.

Assuming the inner coil remains at a constant vertical position z but moves transversally, a change in the outer coil signal V_{diff} as a function of transverse displacement a is interpreted by the seismic attenuation control system as a vertical inner coil displacement. At $z = 2\,mm$ the simulation predicts a change in V_{diff} of $\approx 4\,V/A$ between $a = 0\,mm$ and $a = 6\,mm$ for type F, for type A a change of $\approx 0.5\,V/A$ between $a = 0\,mm$ and $a = 19\,mm$ is simulated. A change of $\approx 4\,V/A$ for type F mimics an inner coil z position shift of $\approx 0.3\,mm$, a signal change of $\approx 0.5\,V/A$ corresponds to a vertical shift of $\approx 0.14\,mm$ for type A. The mimicked inner coil position shift causes the seismic control system to overcompensate the displacement, introducing vibrations to the suspension system. Transversal effects which are unaccounted for may thus actively hinder GW measurement by exciting the pendulum stages.

In real life operating conditions the transverse offset a due to residual motion is expected to remain well below $\approx 1\,mm$, for these offsets ($a = 1\,mm$) only minimal variation in the response is observed; for type F a relative response deviation of $-0.16 \pm 0.33\,\%$ is measured, for type A this equates to $0.31 \pm 0.61\,\%$, both results are compatible with a 0% deviation. Although the residual transversal motion may be limited to $\approx 1\,mm$, these results point out it is important to correctly align the inner coil to the symmetric axis of the outer coils during commissioning in ETpathfinder. Misalignment of the symmetric axis will similarly decrease the linear range for type F as well as increase the response of both LVDT types, which in turn causes overcompensation of the control systems. By taking into account the optimal transversal operating range of LVDTs, the effects of transversal motion can be minimised.

Finally, the comparison between simulation and measurement tests both the developed algorithms and capabilities of the experimental test setup. Probing large offsets of $a = 6\,mm$ and $a = 19\,mm$ for type F and A respectively shows the theoretical and experimental models of the LVDT system align. The test setup allows for accurate measurements of the changes in response by using its vertical and horizontal actuators as well as the laser position sensor. Noise and drift on the data however limit conclusive absolute comparisons of measurements of the differential outer coil signal as a function of the inner coil position.

The overlap between simulation and experiment indicates the simulation can be extended to other LVDT designs and may serve as a guiding line if measurement proves difficult. All ETpathfinder LVDT types may be simulated and experimentally measured to understand their full operating capabilities, while also being improved upon. Voice coil actuators require similar simulations to LVDT sensors, and in conjunction with the dedicated setup at UAntwerpen can be fully characterised. Additionally, completely new sensors based on electromagnetic coils can be designed like reversed LVDTs where the function of the outer and inner coils are switched, corecoil LVDTs which use 3 outer coils and 1 shorted inner coil along with a ferromagnetic core, ... The simulation and experimental setup allows for the

design and testing of truly next generation position sensors, pushing us one step closer to the realisation of the Einstein Telescope.

Bibliography

[1] Albert Einstein. “Näherungsweise Integration der Feldgleichungen der Gravitation”. In: *Sitzungsberichte der Königlich Preussischen Akademie der Wissenschaften (Berlin)* (Jan. 1916), pp. 688–696 (cit. on p. 1).

[2] B. P. Abbott, R. Abbott, T. D. Abbott, et al. “Observation of Gravitational Waves from a Binary Black Hole Merger”. In: *Phys. Rev. Lett.* 116 (6 Feb. 2016), p. 061102 (cit. on pp. 1, 4).

[3] The LIGO Scientific Collaboration, J Aasi, B P Abbott, et al. “Advanced LIGO”. In: *Classical and Quantum Gravity* 32.7 (Mar. 2015), p. 074001 (cit. on p. 1).

[4] F Acernese, M Agathos, K Agatsuma, et al. “Advanced Virgo: a second-generation interferometric gravitational wave detector”. In: *Classical and Quantum Gravity* 32.2 (Dec. 2014), p. 024001 (cit. on p. 1).

[5] The LIGO Scientific Collaboration, the Virgo Collaboration, the KAGRA Collaboration, et al. “GWTC-3: Compact Binary Coalescences Observed by LIGO and Virgo During the Second Part of the Third Observing Run”. In: *arXiv e-prints*, arXiv:2111.03606 (Nov. 2021), arXiv:2111.03606. arXiv: 2111.03606 [gr-qc] (cit. on p. 1).

[6] T. Akutsu, M. Ando, K. Arai, S. Zeidler, and Z.-H. Zhu. “KAGRA: 2.5 generation interferometric gravitational wave detector”. In: *Nature Astronomy* 3.1 (Jan. 2019), pp. 35–40 (cit. on p. 1).

[7] ET Steering Committee Editorial team. *Einstein Telescope design report update 2020*. Tech. rep. ET-0007B-20. ET Steering Committee, 2020 (cit. on pp. 1, 5).

[8] Michele Maggiore, Chris Van Den Broeck, Nicola Bartolo, et al. “Science case for the Einstein telescope”. In: *Journal of Cosmology and Astroparticle Physics* 2020.03 (Mar. 2020), pp. 050–050 (cit. on p. 1).

[9] C J Moore, R H Cole, and C P L Berry. “Gravitational-wave sensitivity curves”. In: *Classical and Quantum Gravity* 32.1 (Dec. 2014), p. 015014 (cit. on pp. 1, 5).

[10] Marica Branchesi, Michele Maggiore, David Alonso, et al. *Science with the Einstein Telescope: a comparison of different designs*. 2023. arXiv: 2303.15923 [gr-qc] (cit. on p. 1).

[11] ETpathfinder team. *ETpathfinder design report*. Tech. rep. ETpathfinder team, 2020 (cit. on pp. 1, 2, 7, 9, 10).

[12] A Utina, A Amato, J Arends, et al. “ETpathfinder: a cryogenic testbed for interferometric gravitational-wave detectors”. In: *Classical and Quantum Gravity* 39.21 (Sept. 2022), p. 215008 (cit. on p. 1).

[13] Halima Tariq, Akiteru Takamori, Flavio Vetrano, et al. “The linear variable differential transformer (LVDT) position sensor for gravitational wave interferometer low-frequency controls”. In: *Nuclear Instruments and Methods in Physics Research Section A: Accelerators, Spectrometers, Detectors and Associated Equipment* 489 (Aug. 2002), pp. 570–576 (cit. on pp. 2, 12, 13, 16).

[14] M.G. Beker, M. Blom, J.F.J. van den Brand, et al. “Seismic Attenuation Technology for the Advanced Virgo Gravitational Wave Detector”. In: *Physics Procedia* 37 (2012). Proceedings of the 2nd International Conference on Technology and Instrumentation in Particle Physics (TIPP 2011), pp. 1389–1397 (cit. on p. 2).

[15] Sean M. Carroll. *Spacetime and Geometry: An Introduction to General Relativity*. Cambridge University Press, 2019 (cit. on p. 3).

[16] James B. Hartle. *Gravity: an introduction to Einstein's general relativity*. 1st. 2003 (cit. on p. 3).

[17] The LIGO Scientific Collaboration, the Virgo Collaboration, the KAGRA Collaboration, et al. *Tests of General Relativity with GWTC-3*. 2021. arXiv: 2112.06861 [gr-qc] (cit. on p. 3).

[18] B. S. Sathyaprakash and Bernard F. Schutz. "Physics, Astrophysics and Cosmology with Gravitational Waves". In: *Living Reviews in Relativity* 12.1 (Mar. 2009) (cit. on p. 4).

[19] K. Riles. "Gravitational waves: Sources, detectors and searches". In: *Progress in Particle and Nuclear Physics* 68 (Jan. 2013), pp. 1–54 (cit. on p. 4).

[20] Xavier Siemens, Jolien Creighton, Irit Maor, et al. "Gravitational wave bursts from cosmic (super)strings: Quantitative analysis and constraints". In: *Physical Review D* 73.10 (May 2006) (cit. on p. 5).

[21] Nelson Christensen. "Stochastic gravitational wave backgrounds". In: *Reports on Progress in Physics* 82.1 (Nov. 2018), p. 016903 (cit. on p. 5).

[22] R. Abbott, T. D. Abbott, S. Abraham, et al. "Upper limits on the isotropic gravitational-wave background from Advanced LIGO and Advanced Virgo's third observing run". In: *Physical Review D* 104.2 (July 2021) (cit. on p. 5).

[23] Zaven Arzoumanian, Paul T. Baker, Harsha Blumer, et al. "The NANOGrav 12.5 yr Data Set: Search for an Isotropic Stochastic Gravitational-wave Background". In: *The Astrophysical Journal Letters* 905.2 (Dec. 2020), p. L34 (cit. on p. 5).

[24] Kamiel Janssens, Guillaume Boileau, Nelson Christensen, Francesca Badaracco, and Nick van Remortel. "Impact of correlated seismic and correlated Newtonian noise on the Einstein Telescope". In: *Physical Review D* 106.4 (Aug. 2022) (cit. on p. 6).

[25] The Virgo Collaboration. *Advanced Virgo Technical Design Report*. Tech. rep. VIR–0128A–12. The Virgo Collaboration, 2012 (cit. on p. 6).

[26] Li-Wei Wei. "Système laser de haute-puissance pour le projet Advanced Virgo : les amplificateurs à fibre combinés de façon cohérente". 2015NICE4091. PhD thesis. 2015 (cit. on p. 6).

[27] F Acernese, M Agathos, K Agatsuma, et al. "Advanced Virgo: a second-generation interferometric gravitational wave detector". In: *Classical and Quantum Gravity* 32.2 (Dec. 2014), p. 024001 (cit. on p. 7).

[28] timothée Accadia, Fausto Acernese, F. Antonucci, et al. "The seismic Superattenuators of the Virgo gravitational waves interferometer". In: *J. Low Freq. Noise Vib. Act. Control* 30 (Jan. 2011), pp. 63–79 (cit. on p. 7).

[29] T. Sekiguchi. "Study of Low Frequency Vibration Isolation System for Large Scale Gravitational Wave Detectors". PhD thesis. Tokyo U., 2016 (cit. on p. 7).

[30] G. Losurdo, M. Bernardini, S. Braccini, et al. "An inverted pendulum preisolator stage for the VIRGO suspension system". In: *Review of Scientific Instruments* 70.5 (May 1999), pp. 2507–2515. eprint: https://pubs.aip.org/aip/rsi/article-pdf/70/5/2507/11077517/2507_1_online.pdf (cit. on p. 8).

[31] A Bertolini, G Cella, R DeSalvo, and V Sannibale. "Seismic noise filters, vertical resonance frequency reduction with geometric anti-springs: a feasibility study". In: *Nuclear Instruments and Methods in Physics Research Section A: Accelerators, Spectrometers, Detectors and Associated Equipment* 435.3 (1999), pp. 475–483 (cit. on p. 8).

[32] Enzo Tapia. *GAS (Geometric Anti Spring) filter and LVDT (Linear Variable Differential Transformer)*. https://gwdoc.icrr.u-tokyo.ac.jp/DocDB/0086/G1808697/001/KAGRA_Lecture2_GAS_filter_and_LVDT.pdf. 2018 (cit. on p. 8).

[33] G. Cella, V. Sannibale, R. DeSalvo, S. Márka, and A. Takamori. "Monolithic geometric anti-spring blades". In: *Nuclear Instruments and Methods in Physics Research Section A: Accelerators, Spectrometers, Detectors and Associated Equipment* 540.2-3 (Mar. 2005), pp. 502–519 (cit. on p. 8).

[34] David J. Griffiths. *Introduction to Electrodynamics*. 4th ed. Cambridge University Press, 2017 (cit. on p. 11).

[35] Wikipedia contributors. *Inductance — Wikipedia, The Free Encyclopedia*. `https://en.wikipedia.org/w/index.php?title=Inductance&oldid=1154394294`. [Online; accessed 26-May-2023]. 2023 (cit. on p. 13).

[36] John David Jackson. *Classical Electrodynamics*. Wiley, 1998 (cit. on p. 14).

[37] Virgilio A. Di and Nucita A.A. *Design of the LVDT Displacement Transducers*. Tech. rep. VIR-NOT-PIS-1390-142. The Virgo Collaboration, Oct. 1999 (cit. on p. 14).

[38] Wikipedia contributors. *Finite element method — Wikipedia, The Free Encyclopedia*. `https://en.wikipedia.org/w/index.php?title=Finite_element_method&oldid=1153781242`. [Online; accessed 27-May-2023]. 2023 (cit. on p. 17).

[39] David Meeker. *Finite Element Method Magnetics*. Version 4.2. May 2020 (cit. on p. 17).

[40] David Meeker. *pyfemm 0.1.3*. Version 0.1.3. July 21, 2021 (cit. on p. 17).

[41] Ku H.H. "Notes on the use of propagation of error formulas". In: *Journal of Research of the National Bureau of Standards* 70C.4 (Oct. 1966), p. 263 (cit. on p. 34).

[42] Paolo Chiggiato. *Outgassing properties of vacuum materials for particle accelerators*. 2020. arXiv: `2006.07124 [physics.acc-ph]` (cit. on p. 39).

List of Figures

List of Tables